November 3, 2011

# Multiple Inverse Method Software Package

# User's Guide

**Atsushi YAMAJI, Katsushi SATO**
Division of Earth and Planetary Sciences,
Kyoto University, Japan

**Makoto OTSUBO**
Institute of Geology and Geoinformation,
National Institute of Advanced Industrial Science and Technology, Japan

# Contents

Slickenfiber lineation on a fault plane in a Cretaceous formation, Wakayama, Japan.

## Copyright



## Disclaimer of warranty

This software package is free.

Free of charge software is provided on an “AS IS” basis, without warranty of any kind, including limitation the warranties of merchantability, fitness for a particular purpose and non-infringement. The entire risk as to the quality and performance of the software is borne by you. Should the software prove defective, you assume the entire cost of any service and repair.

## Acknowledgments

We are grateful to our coworkers and the researchers who tested and/or utilized the multiple inverse method. Discussions with the members of the Earthquake Research Institute cooperative research program were fruitful for the adaptation of the method to earthquake focal mechanisms. Thanks are also due to the Japan Society for the Promotion of Science for the Grant-in-Aid for Scientific Research, (C)(2)14540423, the grant from which was used to improve and release the software package.

# 1 Introduction

What is the multiple inverse method? The method is a numerical technique to separate stresses from heterogeneous fault-slip data [46] and from heterogeneous focal mechanism data [30]. The former class of data are obtained from outcrops, borehole cores, etc., and allows us to understand secular changes in crustal stress. The latter class of data come from seismic events, and cast light on spatial and/or temporal changes in the state of stress at depths.

This document describes the way to use the software package implementing the multiple inverse method for the Windows Operating System. The mechanism of the method is explained in Appendix C of this document and in the articles [29, 30, 46].

## 1.1 Purpose of this software package

What are *heterogeneous* fault-slip data? The heterogeneity is the key term for the method. First, we assume that stresses with the common principal orientations and the common stress ratio represent the a state of stress. Then, suppose that an area experienced two successive ages with different stress states, and that a group of faults was activated by the older stress state and another one by younger stress state. It is not straightforward to determine the geological age of fault movement. So, suppose further that we cannot discriminate between between the groups. Then, the fault-slip data from all the faults are said to be heterogeneous. In contrast, the data only from one of the groups are said to be homogeneous, and bear the information of the stress state corresponding to the specific group of faults. A heterogeneous data set comes also from a rock mass in which the state of stress changes spatially and/or temporarily.

If a homogeneous data set is given, it is very easy to determine the stress that was responsible for the faulting or seismic events by means of the classical stress inversion method (Appendix B.7), which was completed until the early 1980s [1, 2, 8, 11, 40]. It is explained in §7.1 to deal with such a dataset with this program package.

The multiple inverse method aims at separating stresses numerically from heterogeneous data. Given a homogeneous data set, the method answers not only the optimal solution but also its confidence level. When a researcher aims at understanding the temporal or spatial changes in the state of stress from a fault-slip or focal mechanism data set, the researcher should expect the heterogeneity of the data set.

## 1.2 Studies using this method

The basic mechanism of the multiple inverse method was proposed in 2000 [46], and was applied to faults in Mesozoic and Cenozoic basins in Japan [14, 15, 17, 18, 36, 45]. After the software became open for the public in 2004, the method was used in various areas in various tectonic settings. Those include faults in Cenozoic rocks around the Baikal Rift, and in northern Iran and western Himalaya [9, 10, 20, 21, 32]; Mesozoic, Paleozoic and Proterozoic rocks in Europe [12, 35, 42]; and a Cenozoic ophiolite in southern Chile [41]. Several researchers used the method to understand processes at depths in metamorphic and accretion complexes [23, 26] and in a wide shear zone [4]. Shear planes in oriented core samples were inverted by the present method to study paleostresses as well [28, 44].

It was difficult to deal with heterogeneous focal mechanism data, because it is not straightforward to determine which of the two nodal planes of a mechanism represents the fault plane, though the nodal plane selections are feasible. Recently, Hiratsuka and Sato assumed both planes being fault planes to infer the stress field around the rapture zone of the 2004 Indian Ocean Earthquake with the multiple inverse method, whereas Pasquale et al. applied the method to the data for verifying this selection [13, 31]. Now, the latest version of this software has the function to deal with heterogeneous focal mechanisms avoiding the selection [30].

## 1.3 About the software package

This software package consists of the main and post processors, sample datasets, User's Guides and auxiliary files. Given a set of geological or seismological data, the main processor calculates stresses that are consistent with the data. The post processor not only visualizes the stresses but also provides various functions to analyze the data and stresses. Using the functions, the user can interactively determine stresses from data, and can classify faults according to the stresses. The method of using the functions is explained in §5.4, and worked problems to determine stresses from homogeneous and heterogeneous data is illustrated in §7. If some faults are observed to cut other faults at an outcrop, we are able to determine the order of faulting. And, we can estimate the time

sequence of the stress states that are thought to be responsible for the faults. Bedding tilt test [51] can be applied to fault-slip data from fold zones or tilted fault blocks by means of the multiple inverse method in tandem with the software "KUT" [37], which untilts fault-slip data and is available from our web site.

### Important Terms

Multiple inverse method
: A numerical technique for detecting stress states from heterogeneous data obtained from geological faults or from seismic focal mechanisms.

Stress state or state of stress
: A state of stress or a stress state represents the stresses that have the same principal orientations and the same stress ratio (Appendix B.2). A stress state is specified by the combination of principal orientations and the value of stress ratio. Note that this diction is not in common use among researchers.

homogeneous data
: If fault activities occur in spatially and/or temporarily homogeneous stress field, data from the activities are said to be homogeneous.

heterogeneous data
: If fault activities occur in spatially and/or temporarily heterogeneous stress field, data from the activities are said to be heterogeneous. It is expected that the heterogeneous stress field is recognized from a heterogeneous data set.

Misfit angle
: The angle between observed and theoretical slip directions on a fault plane. The latter is obtained from an assumed stress state.

# 2 Evolution of the method

The multiple inverse method was invented in the late 1990s [45]. And, the software implementing the method became open to the public in 2004. At that time, both the main and post processors had the version number 4.

## 2.1 Main processor

The alteration from the version 3 to 4 was due to the improvement in the computational grid by [34], which was realized by the redefinition of the parameter space to represent stress states [33].

The main processor version 5 had improved algorithm to reduce noises to improve resolution, and to shorten the time of computation [29]. The improvement of the main processor to the version 6 includes mainly the function to deal with heterogeneous focal mechanism data [30]. There is no change in the function to deal with geological fault-slip data. But, the recent refinement of the computational grid improved the resolution of the method [50].

The article [29] reports the resolution of the main processor version 5 using artificial data sets[1]. Another article [30] briefly reports the resolution of the main processor version 6 when it is applied to heterogeneous focal mechanisms.

Paired stereograms in Fig. 1 illustrate the difference in the resolution of the versions applied to the identical heterogeneous dataset that were artifically generated with the assumed stresses A and B. Because of those gradual improvement, it is advisable for the users to specify the version number of the main processor in their articles.

## 2.2 Post-processor

Unlike the main processor, there have been no important changes since 2004, except for the alterations of the Stress menu. Until the version 4.14, this menu included the functions of measurements and visualization methods. Functions of the first category are included by the Measurement menu of the present version of the post processor (ver. 4.15). Those of the second category are moved to the newly-established View menu. The Stress menu ceased to exist. In addition, the version 4.15 got the function to measure the angular stress distance (Appendix B.5) between the stress states that the user specifies on the main window of the program. The present one (version 4.16) has the function to draw Mohr diagrams for triaxial stresses, which the user specifies. The normal and shear stresses on fault planes are plotted on the digrams as well.

# 3 Installation

The minimum system requirements for this program package are listed below.

[1] Liesa and Lisle [19] tested the resolution and accuracy of the main processor version 4.

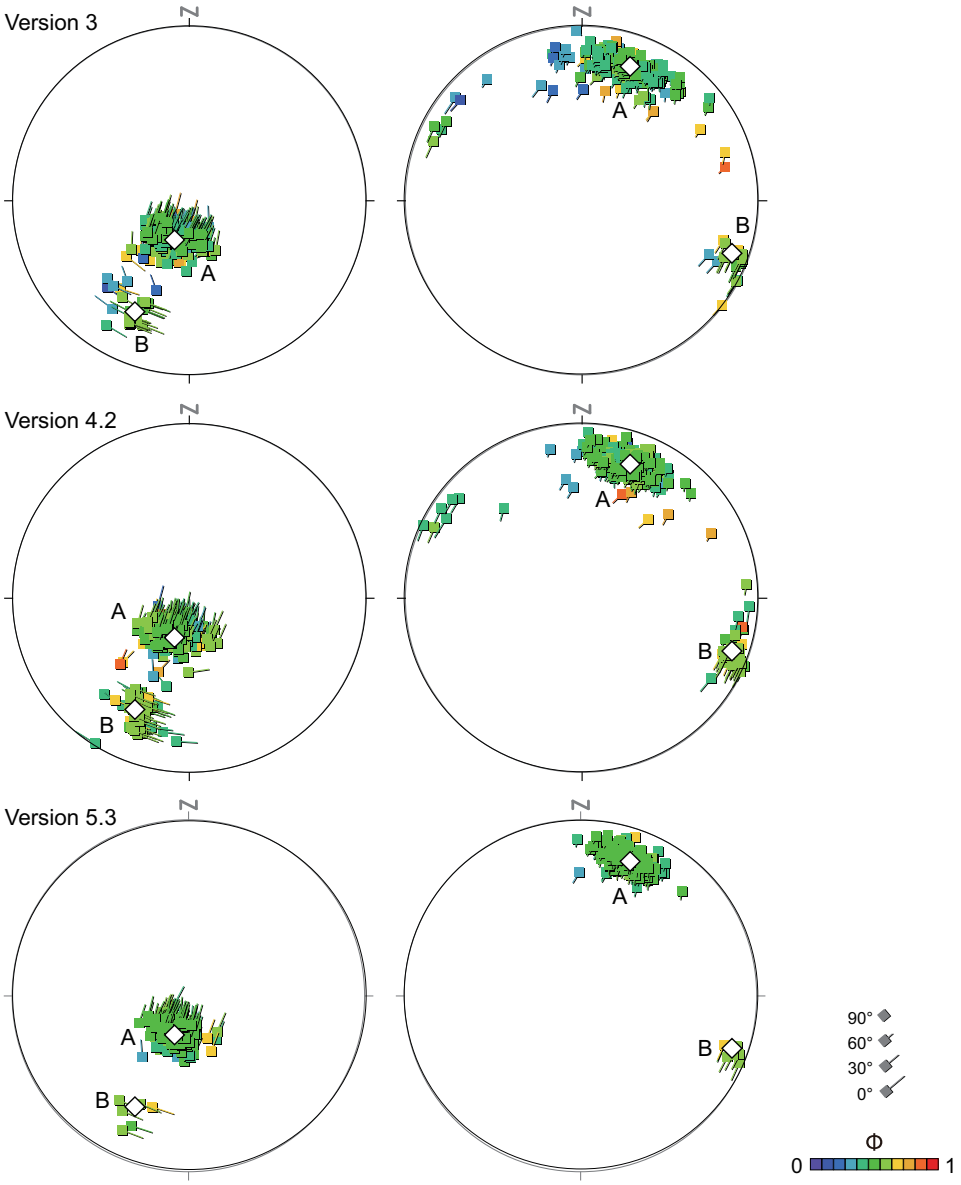


Figure 1: Paired stereograms showing the results of the different version of the main processor obtained from a set of artificial heterogeneous fault-slip data with the parameters, $k = 5$ and $e = 6$. Open diamonds indicate the principal orientations of the assumed stresses. The stressed A and B had the stress ratios of 0.5 and 0.6, respectively. Lower-hemisphere, equal-area projections.

- Pentium processor, 200 MHz
- 200 MB RAM
- 7 MB free disk space
- Pointing device (mouse)
- Windows 98/NT4

In short, the software runs on a PC circa 2000. The software is compatible with Windows 7 and with Windows x64 Edition. A Macintosh user reported the compatibility of the software with Parallels Desktop[2].

It is very easy to install the package in your computer, as the installation does not change the registry of the Windows Operating System. The package is available from the web site[3],

www.kueps.kyoto-u.ac.jp/ web-bs/tsg/software/

[2]Parallels Desktop is Macintosh software by Parallels, Inc., providing hardware virtualization for Macintosh computers with Intel processors.

[3]If the above site is not found, please visit one the home pages of the authors.

Download the zipped file from this site, and and extract files from it in a directory in your computer[4]. Then, you can use the software.

The executable files `mim60.exe` and `miv4.exe` are the main and post processors. It is possible to launch the executable files from the Start menu of the Windows Operating System. Consult the built in help system of your operating system for the procedure to register the executable files in the menu.

Uninstallation is easy as well. Just delete the directory containing the software package.

# 4 Main processor

This software package includes the executable files `mim4.exe` and `mim60.exe`, which correspond to the versions 4 and 6 of the main processor. The former is provided exclusively for the purpose of the bedding tilt test proposed that we proposed for paleo-stress analysis of fault-slip data from tilted rocks [51]. Use the version 6 unless the user apply the test. The usage of the both programs are basically the same. So, we explain only the latest version of the main processor in this section.

The main processor reads a data file in a certain format (§6), and outputs the result in a text file, which is visualized by the post processor.

## 4.1 Basic operations

The main processor, `mim60.exe`, is a console program (Fig. 2). The following is the procedure to use the main processor.

1. Double-click on the icon of the executable file to launch the program. The program can be launched through a console window opened beforehand.

2. As soon as the executable file is launched, an open dialog pops up to prompt the user to select a data file. Choose an appropriate data file.

3. Next, specify an output file name through a save dialog. The program appends automatically the file extension `mi4`. If the user specifies an existing file, the program asks to input the character "y" or "n" on the console window to answer yes or no to confirm or cancel the overwriting. If canceled, the program is terminated.

4. Input an integer 1 or 2 to indicate either geological fault-slip data or seismological focal mechanism data are processed (Fig. 2).

5. Input an integer for the fault combination number, $k$, through the console window. The data classes have different range of $k$. For fault-slip data from geological faults, the program accepts an integer in the range $3 \leq k \leq 8$. Input one of these numbers following the prompt `k =`. For the case of focal mechanism data, input an integer following the prompt `k <4 or 5> =`. The program accepts the value 4 or 5. We recommend the value $k = 5$. If the number of data is as large as, say, $> 100$, $k = 4$ is acceptable[5].

Having received all the parameters above, the program echoes back the file names as

```
Input  :  sample_fm.fdt
Output :  sample_fm_v6k5.mi5
```

The fraction `4800 / 487635` at the final line of the console window in Fig. 2 shows the progress of the computation, and indicates that $4800/487635 \approx 1\%$ of the entire computation had done. The numerator increases by hundreds. The denominator of the fraction above equals the binomial coefficient,

$$ {}_N\mathrm{C}_k = \frac{N!}{k!(N-k)!}, $$

where $N$ is the number of faults, or equals

$$ {}_{2N}\mathrm{C}_k = \frac{(2N)!}{k!(2N-k)!}, $$

where $N$ is the number of focal mechanisms. The user can predict when the computation ends by comparing the increasing fraction.

Shortly after all the computation is over, the main processor writes the result in the output file, and closes the console window. If the user launch the program through a console window opened beforehand, he or she can read the messages from the main processor.

The execution is canceled by clicking on  at the upper-right corner of the window.

We recommend $k = 5$. If $N$ is large, $k = 4$ is appropriate. The main processor has the maximum number of faults, $N_{\max}$ that the processor can handle. $N_{\max}$ depends on $k$ (Table 4.2).

[4] Avoid characters other than alpha-numeric ASCII characters for the directory names of this software package

[5] The present version of the program has the upper bound for the number of data (Table 4.2).

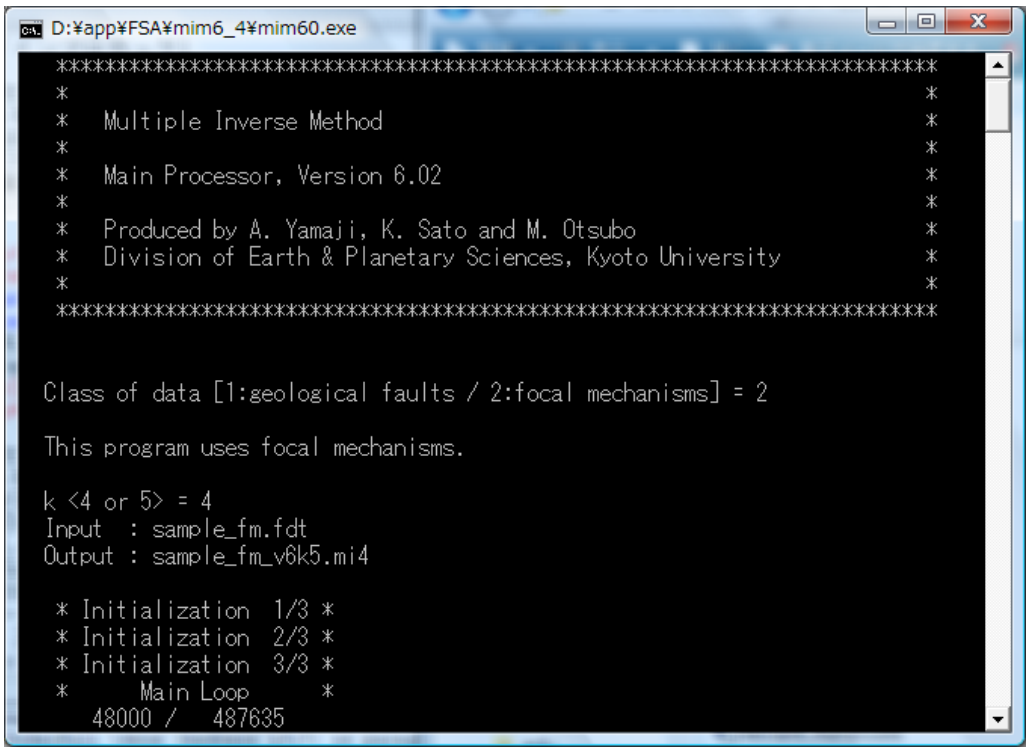


Figure 2: Console window of the main processor.

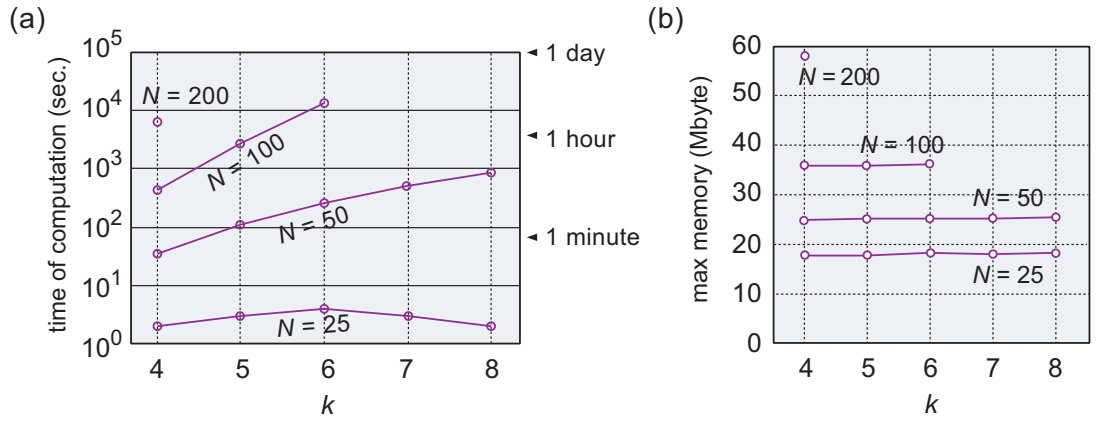


Figure 3: Time of computation and memory needed by the main processor for calculation. The data shown here were measured with a personal computer (Pentium IV, 2.4 GHz, 512 M bytes of memory).

## 4.2 Computational resources

The present version of the main processor has the limitation in the number of faults, $N$, so as to satisfy the inequality, ${}_N\mathrm{C}_k < 2,147,483,647 = 2^{31}$, because the program uses 32-bit signed integers to count the iterations. For the case of focal mechanism data, the condition ${}_{2N}\mathrm{C}_k < 2,147,483,647$ must be meet, where $N$ is the number of data. This limitation will be removed in a future version by utilizing 64-bit ones. If $N$ is large, specify a smaller $k$ not to exceed the upper bound (Table 4.2).

The time of computation depends on data in two ways, the number and heterogeneity of data. The processing of focal mechanism data takes about twice the longer time of computation than that of geological fault-slip data. The following is the explanation of the time for the latter class of data.

First, the time of computation depends on the $k$ value that the user choose and on $N$, the number of

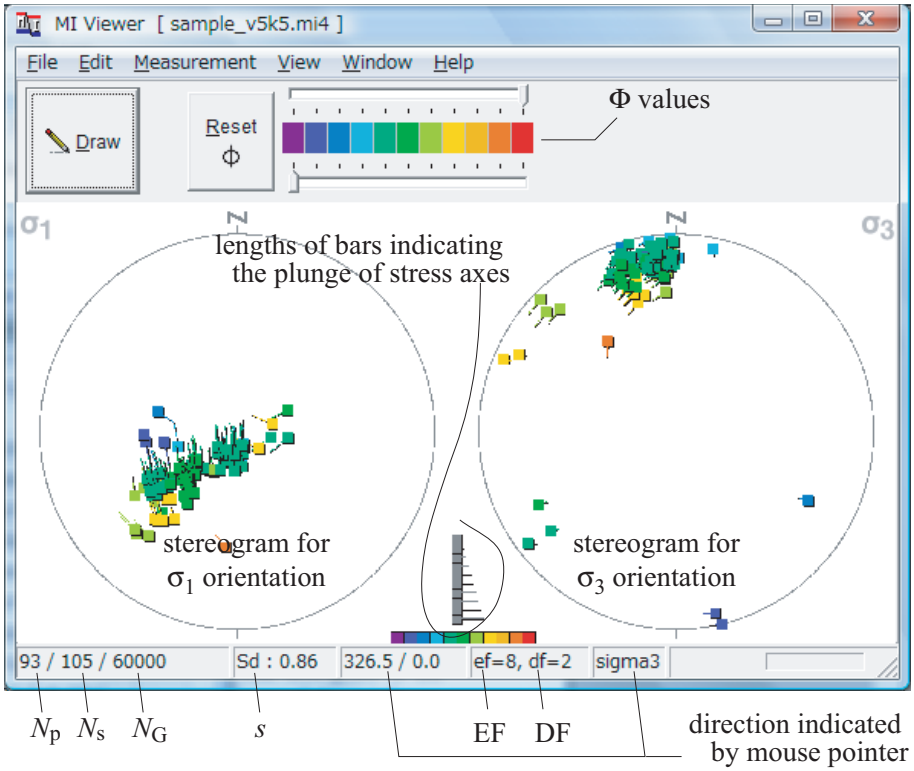


Figure 4: Main window of the post processor. Stress states significant for data are visualized as clusters on the paired stereograms; principal orientations of the stresses are denoted by lower-hemisphere, equal-area projection. $N_p$, the number of stress states plotted on each stereogram; $N_s$, the number of different stress states output by the main processor; $N_G$, the number of computational grid points used by the processors; EF, enhance factor; DF, dispersion factor.

faults. Given these parameters, the program iterates the classical stress tensor inversion (p. 28) many times. The number of iteration is smaller than or equal to ${}_N\mathrm{C}_k$. As $k$ is generally smaller than $N$ by at least one order of magnitude, ${}_N\mathrm{C}_k$ is approximated by $N^k$, which inflate with increasing $N$ and $k$.

Second, how the actual number of iteration is reduced from ${}_N\mathrm{C}_k$ depends on the heterogeneity of data[6]. The more heterogeneous the data are, the smaller the number is. Fig. 3(a) shows the time of computation for an artificial data set. The decrease in the time of computation for the case of $N = 25$ and $k > 6$ resulted from the reduction effect.

Table 1: The fault combination number $k$ and the corresponding maximum number of data $N_{max}$ the main processor can handle. FSD, fault-slip data; FMD, focal mechanism data.

| $k$ | 3 | 4 | 5 | 6 | 7 | 8 |
|---|---|---|---|---|---|---|
| FSD | 499 | 269 | 122 | 75 | 55 | 44 |
| FMD | | 238 | 96 | | | |

# 5 Post Processor

The post processor has various functions, among which the main is to visualize the results that the main processor calculated from data sets. In this section, the procedure for the visualization is briefly explained. Other functions are detailed in §5.3.

## 5.1 Basic operations

The post processor has the name “MI Viewer”, and the executable file `miv4.exe`. The program has the main and data windows, the former of which shows this name in the title bar of the window (Fig. 4). The latter has the title Fault-Slip Data in the title bars (Fig. 5).

[6]The main processor version 4 and earlier versions iterated the classical stress inversion literally ${}_N\mathrm{C}_k$ times [46]. Adopting the algorithm of Otsubo and Yamaji [29], the program cuts back on the number of iterations after the version 5.

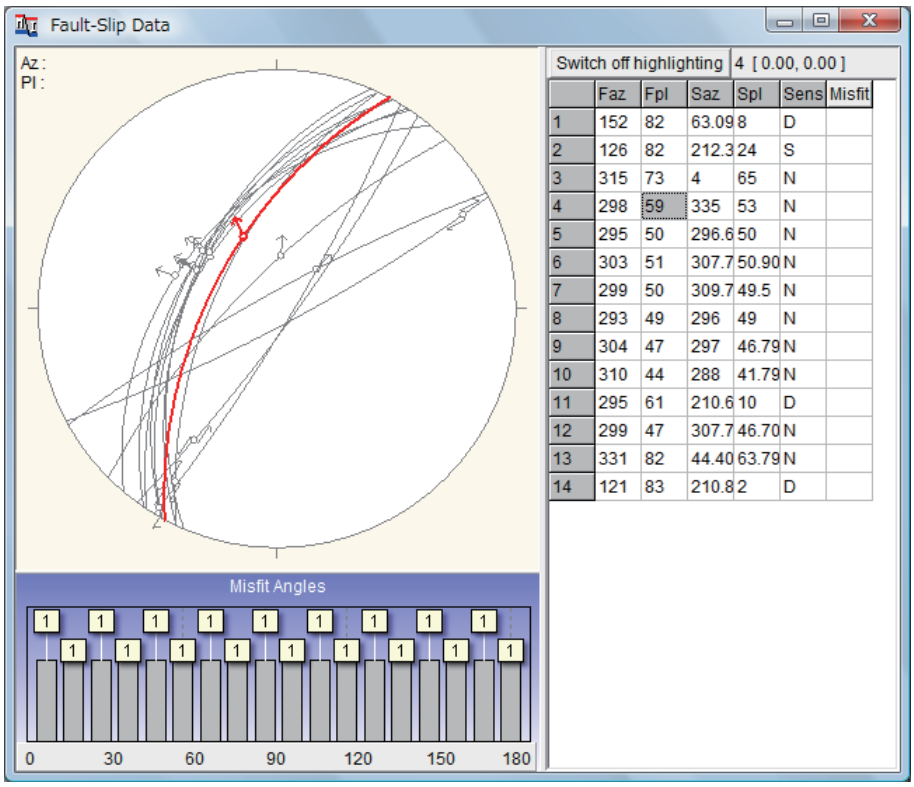


| | Faz | Fpl | Saz | Spl | Sens | Misfit |
|---|---|---|---|---|---|---|
| 1 | 152 | 82 | 63.09 | 8 | D | |
| 2 | 126 | 82 | 212.3 | 24 | S | |
| 3 | 315 | 73 | 4 | 65 | N | |
| 4 | 298 | 59 | 335 | 53 | N | |
| 5 | 295 | 50 | 296.6 | 50 | N | |
| 6 | 303 | 51 | 307.7 | 50.90 | N | |
| 7 | 299 | 50 | 309.7 | 49.5 | N | |
| 8 | 293 | 49 | 296 | 49 | N | |
| 9 | 304 | 47 | 297 | 46.79 | N | |
| 10 | 310 | 44 | 288 | 41.79 | N | |
| 11 | 295 | 61 | 210.6 | 10 | D | |
| 12 | 299 | 47 | 307.7 | 46.70 | N | |
| 13 | 331 | 82 | 44.40 | 63.79 | N | |
| 14 | 121 | 83 | 210.8 | 2 | D | |

Figure 5: Data window of the post processor. The table in this window shows the fault-slip data processed by the present method. The same data are illustrated by the lower-hemisphere stereonet. One fault datum is high lighted by red lines in the stereonet, because the datum is indicated at the first line in the list and the first column of the line had been clicked. The column is high lighted by gray background.

When the post processor is launched, the main window lies on the data window. Choose items in the Window menu on the main window or type Alt+W on the keyboard to bring the data window on the main one.

Follow the steps below for the visualization.

1. Run the executable file `miv4.exe`.

2. Choose one of the files that were output by the main processor by clicking the File menu and then the Open submenu on the main window. An open dialogue opens by these operations. If the file is loaded, the fault-slip data that are contained in the file are shown on the data window.

3. Click the Draw button on the main window, then the result of the multiple inverse method applied to the fault-slip data is visualized on the paired stereograms on the main window (Fig. 4).

4. Click the File menu and click the menu item Exit to terminate the program.

## 5.2 Visualization

The post processor visualizes the results of the multiple inverse method, and extracts the pieces of information about the stress states recorded in the user's data.

### 5.2.1 Main window

The paired stereograms on the main window show the principal orientations of the stresses detected by the multiple inverse method (Fig. 4). The stereograms use lower-hemisphere, equal-area projection. Each of the symbols that have heads and tails like tadpoles plotted on the stereograms represents a state of stress. A state of stress or a stress state represents stresses with the common principal orientations and the common values of stress ratio. In what follows, we use the term "tadpole symbols" for them (Fig. 6).

Clusters of tadpole symbols with similar colors and similar attitudes on the stereograms represent significant stresses for a given set of fault-slip data. The stresses detected from heterogeneous data are de-

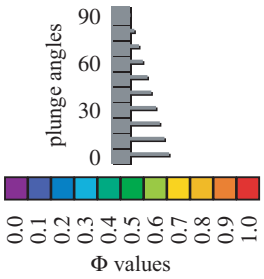


Figure 6: The legend plotted between the paired stereograms in the main window. The plunge of stress axes are denoted by the lengths of the tails of tadpole symbols. Φ values are color coded with the intervals of 0.1.

picted by those clusters.

A color of the symbols denotes the stress ratio,

$$\Phi = \frac{\sigma_2 - \sigma_3}{\sigma_1 - \sigma_3}, \qquad (1)$$

where $\sigma_1$, $\sigma_2$ and $\sigma_3$ are principal stresses and $\sigma_3 \leq \sigma_2 \leq \sigma_1$. We use the sign convention that compression is positive. By definition, the value of $\Phi$ has the range [0, 1]. The two cases $\Phi = 0$ and 1 represent the stress states $\sigma_1 > \sigma_2 = \sigma_3$ and $\sigma_1 = \sigma_2 > \sigma_3$, respectively. Both of these are axial stresses. Triaxial stresses have intermediate $\Phi$ values, Values of this ratio are indicated by 11 colors with an interval of 0.1. There are color bars just below the menu bar and under the stereograms. The color scheme can be freely changed. Violet and red indicate $\Phi = 0$ and 1, respectively, in Fig. 4. And, for example, $\Phi = 0.2$ is represented by the third color from the left in the color bar. $\Phi$ values are digitized with the intervals of every 0.1 on the main window. Each of the color bars on the right-hand side of the Reset button and under the paired stereograms are composed by 11 colors (Fig. 4), and indicate the color coding of the 11 $\Phi$ values 0.0, 0.1, . . . , and 1.0.

A state of stress is completely depicted by a tadpole symbol on one of the paired stereograms as follows, but the use of two stereograms help a user discern the principal orientations of the state of stress (Fig. 7). On the left stereogram, position of the head of a tadpole symbol indicate a $\sigma_1$ orientation, and the azimuth and plunge of the $\sigma_3$ orientation is designated by its tail (Fig. 6). The length of a tail is drawn proportional to the difference between 90° and the plunge of the $\sigma_3$ axis. The steeper the $\sigma_3$-axis, the shorter the tail is. The correspondence between the length and plunge is shown by the ten gray tadpole symbols plotted between the stereograms; they indicate the plunges at 0°, 10°, 20°, . . . , and 90°. The roles of the head and tail of each tadpole symbol are inverted on the right stereogram. That is, the position of the head of a tadpole symbol on the stereogram indicates the $\sigma_3$ orientation; and the length and direction of the tail denote the plunge and azimuth of $\sigma_1$ orientation. Using the two stereograms the user can easily take in the stress states that are represented by the cluster of tadpole symbols.

At the base of the main window, a status bar indicate several parameters. Among those, the string sigma3 in Fig. 4 indicates that the mouse pointer was placed on the right stereogram, and the fraction 31.1 / 0.0 indicates that the position of the pointer corresponded to the azimuth at 31.1° and the plunge at 0.0° when the picture was captured. Other items shown in the status bar are explained in the next section.

The track bars above and below the color bar on the right-hand side of the Draw button are used to limit the range of $\Phi$ values of the stress states to be plotted on the stereograms. Track bars 1 and 2 in Fig. 8 indicate the upper and lower bounds of the values.

### 5.2.2 Data window

The data window has three panels (Fig. 5). Fault-slip data are shown in the stereonet occupying the upper left panel. At the upper left corner of this panel, the position of the mouse pointer is shown by the azimuth and plunge of the position on the stereonet. List of the data are shown in the panel to the right of the stereonet. When the program deals with geological fault-slip data, each row in the list corresponds a fault-slip datum. If the method is applied to focal mechanism data, two succeeding rows indicate the parameters of the nodal planes of a focal mechanism datum corresponding to a seismic event.

The pop-up window in Fig. 9 appears by right-clicking on the data window. The fault-slip data in Fig. 5 are exhibited by their tangent-lineation diagram in Fig. 10. The plotting methods can be switched by choosing the two submenu items under Plot Method of the pop-up menu.

If a line in the list is clicked, the corresponding fault is highlighted by red lines on the stereonet. Just before the window shown in Fig. 5 was captured, the first datum in the list had been clicked. It is easy to see the correspondence between plotted symbols in the stereonet and data in the list. Function of the button Switch off highlighting is literally to switch off the highlighting.

The bar graph in the lower left panel shows the his-

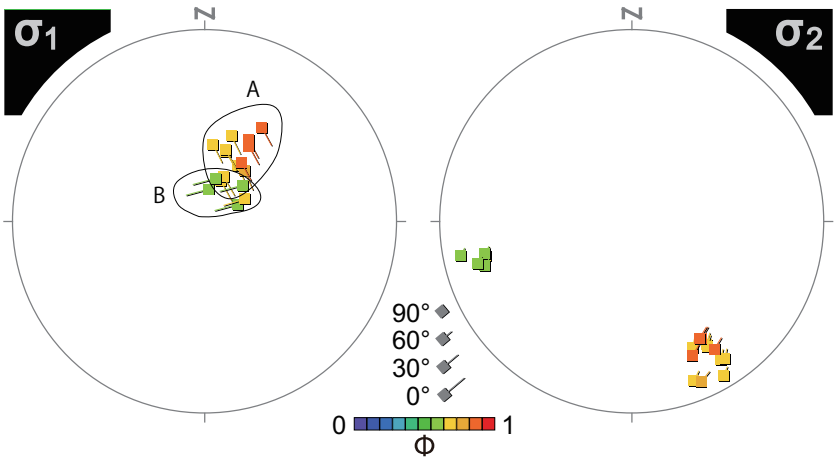


Figure 7: Even without colors, the correspondences of the clusters A and B in the two stereograms turns out from the lengths and directions of tadpole tales.

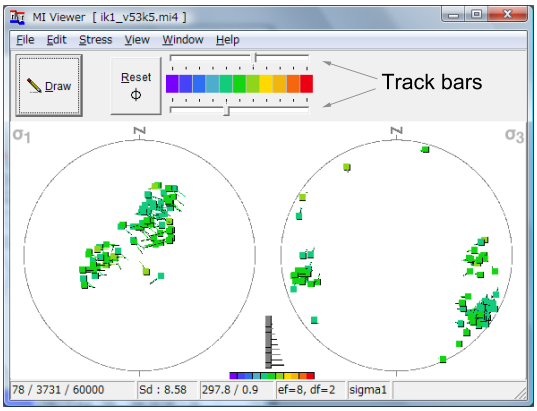


Figure 8: Track bars above and below the color bar limits the rage of Φ values plotted on the stereograms. When this picture was captured, the stress states with Φ = 0.4–0.6 were plotted on the paired stereograms.

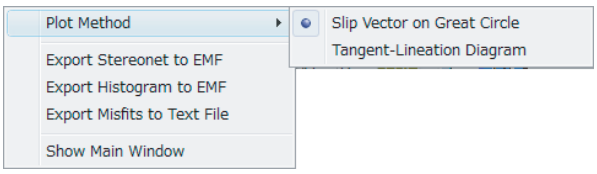


Figure 9: The pop-up window shown by right-clicking on the data window.

togram of the angular misfits between observed and theoretical slip directions of the faults. The latter directions are calculated with a state of stress designated on the main window. The usage of this histogram is explained in the next subsection (p. 10).

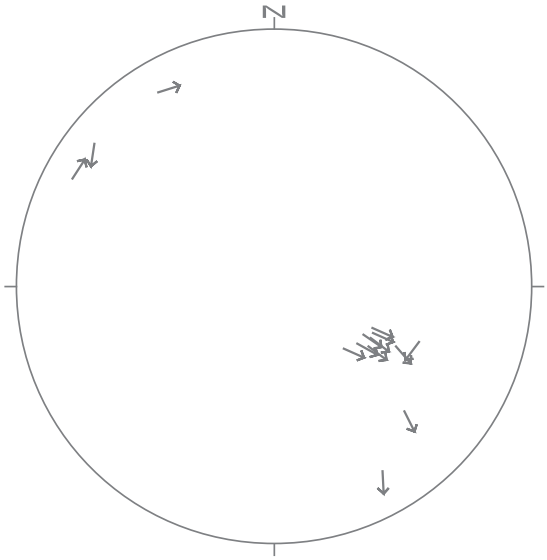


Figure 10: Tangent-lineation diagram showing the fault-slip data in Fig. 5.

## 5.3 Menu items

The post processor has various functions to help analysis. The user can use the functions interactively through the main and data windows.

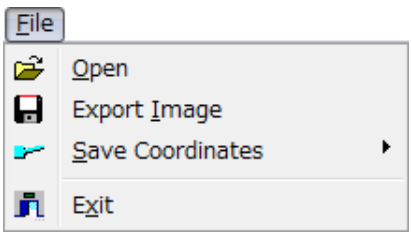

### 5.3.1 File menu

First time the user launch the post processor, the last item in the File menu is Exit. If a file is loaded, the file name is automatically recorded in the text file `prevfiles.txt`, which is stored in the home directory of the post processor. Next time you launch the program, the file names are appended below Exit as dynamically created menu items, with which the user can access to the files.

**[Open]** Click Open to load a file that was output by the main processor. The data in the file is not plotted on the paired stereograms until the Draw button on the main window is clicked.

**[Export Image]** The paired stereograms are saved as a vector or raster image in a file with the extension `emf` or `jgp`, respectively, through this menu item in order for publication.

**[Save Coordinates]** The stress states depicted by tadpole symbols are exported in a text file through this menu item, which has the submenu items Principal axes and stress ratios and Reduced Stress Tensors. When the former is chosen, the azimuth and plunge of the $\sigma_1$- and $\sigma_3$-axes and the stress ratios are saved. Each line in the text file corresponds to one tadpole symbol. If the latter is chosen, the six components of the reduced stress tensors (p. 25) representing the stress states, $\sigma_{11}$, $\sigma_{12}$, $\sigma_{13}$, $\sigma_{22}$, $\sigma_{23}$ and $\sigma_{33}$ are saved[7], where we use the rectangular Cartesian coordinates in Fig. 38. Six items in a row in the file are the values of these components in this order.

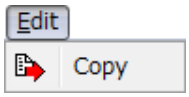


### 5.3.2 Edit menu

**[Copy]** The graphics shown on the paired stereograms is stored in the clipboard by choosing the Copy item from the Edit menu. The user can edit the picture with a drawing software.

### 5.3.3 Measurement menu

Functions for measuring misfit angles and statistics of stress states are accessible from Measurement menu.

[7]The version 4.10 and earlier of MI Viewer output components of the reduced stress tensors defined by Orife and Lisle [25], which are equal with the components of the tensor in Eq. (6) multiplied by $\sqrt{2/3}$.

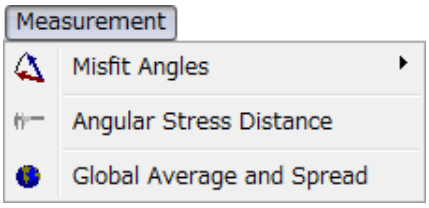


**[Misfit Angles]** The post processor has the function of calculating the theoretical slip directions of faults based on the Wallace-Bott hypothesis (Eq. 4, p. 24) for the state of stress specified by the user (Fig. 11). The angular misfits between theoretical and observed ones are also computed. The misfit angles are used as the keys to classify data (§7).

The user have to specify $\sigma_1$- and $\sigma_3$-orientations and a value of $\Phi$ to input a state of stress. The main window receives these parameters through three steps.

1. Designation of one of the orientations.
2. Designation of the remaining orientation.
3. Designation of a $\Phi$ value.

The menu item Misfit Angles has two submenu items, Designate by Mouse and Designate an Axis through Keyboard (Fig. 12) to prompt the user to choose one of the two ways for designating the first orientation.

If the submenu item Designate by Mouse is chosen, the tip of the mouse pointer is encircled on the main window (Fig. 13). And, the status bar shows the sign Designate 1st Axis, indicating that the program is in the first mode to designate the stress axis the user is going to specify. The open circle moves with the tip of the mouse pointer. In Fig. 13 the pointer is placed on the left stereogram, meanwhile, the great circle arc on the plane perpendicular to the direction indicated by the pointer is drawn on another stereogram. The arc moves following the movement of the mouse pointer. Place the circle on a cluster, then click the left mouse button to designate the principal orientation. This operation fixes the open circle and the arc, and cues the program in entering the second mode to designate another stress axis.

If the submenu item Designate an Axis through Keyboard is chosen (Fig. 12), the panel in Fig. 14 appears to prompt the user to input the $\sigma_1$- or $\sigma_3$-orientation through the keyboard. Input the azimuth and plunge of the $\sigma_1$- or $\sigma_3$-axis, and click on the Confirm Parameters button to terminate the first mode. The other stress axis and stress ratio are designated by the same steps with those described in the explanation of the menu item Designate by Mouse. The

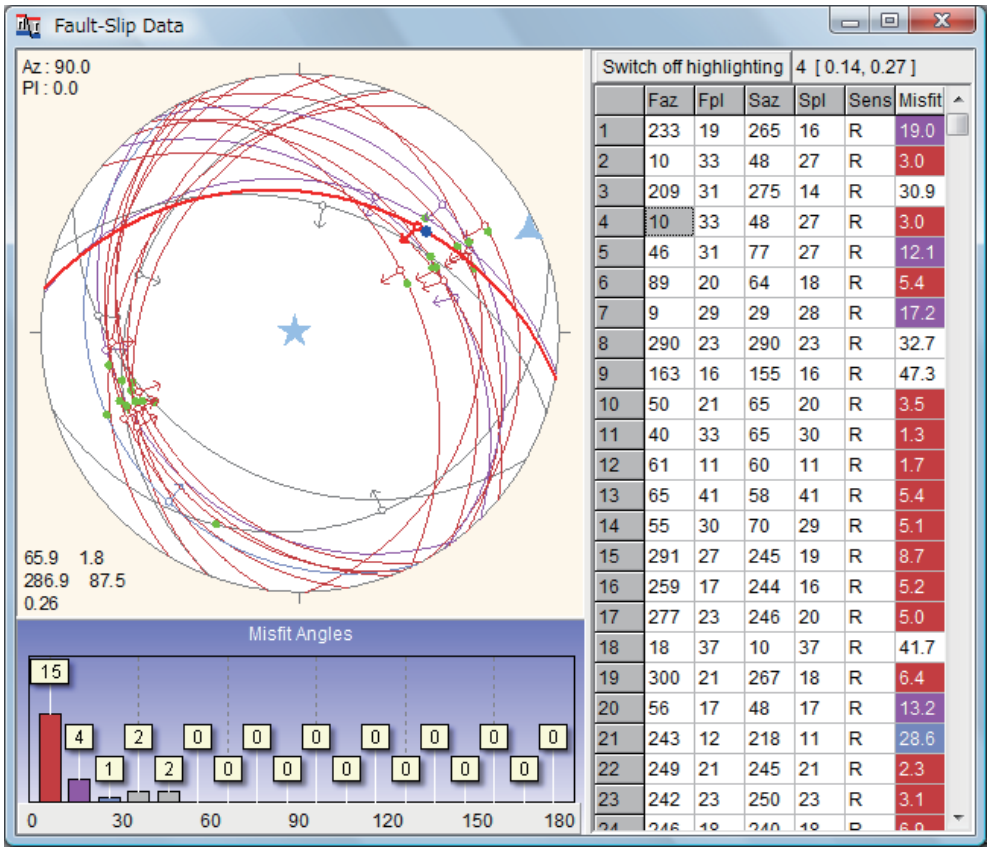


| | Faz | Fpl | Saz | Spl | Sens | Misfit |
|---|---|---|---|---|---|---|
| 1 | 233 | 19 | 265 | 16 | R | 19.0 |
| 2 | 10 | 33 | 48 | 27 | R | 3.0 |
| 3 | 209 | 31 | 275 | 14 | R | 30.9 |
| 4 | 10 | 33 | 48 | 27 | R | 3.0 |
| 5 | 46 | 31 | 77 | 27 | R | 12.1 |
| 6 | 89 | 20 | 64 | 18 | R | 5.4 |
| 7 | 9 | 29 | 29 | 28 | R | 17.2 |
| 8 | 290 | 23 | 290 | 23 | R | 32.7 |
| 9 | 163 | 16 | 155 | 16 | R | 47.3 |
| 10 | 50 | 21 | 65 | 20 | R | 3.5 |
| 11 | 40 | 33 | 65 | 30 | R | 1.3 |
| 12 | 61 | 11 | 60 | 11 | R | 1.7 |
| 13 | 65 | 41 | 58 | 41 | R | 5.4 |
| 14 | 55 | 30 | 70 | 29 | R | 5.1 |
| 15 | 291 | 27 | 245 | 19 | R | 8.7 |
| 16 | 259 | 17 | 244 | 16 | R | 5.2 |
| 17 | 277 | 23 | 246 | 20 | R | 5.0 |
| 18 | 18 | 37 | 10 | 37 | R | 41.7 |
| 19 | 300 | 21 | 267 | 18 | R | 6.4 |
| 20 | 56 | 17 | 48 | 17 | R | 13.2 |
| 21 | 243 | 12 | 218 | 11 | R | 28.6 |
| 22 | 249 | 21 | 245 | 21 | R | 2.3 |
| 23 | 242 | 23 | 250 | 23 | R | 3.1 |

Figure 11: Data window after a state of stress is designated through the main window: the stress has the stress ratio $\Phi = 0.3$ and the $\sigma_1$ and $\sigma_3$ orientations indicated by the symbols ▲ and ★, respectively, on the stereonet. The orientations and the stress ratio are shown by their azimuths and plunges at the lower left of the net. The lower left panel shows the histogram of misfit angles for this stress. Bars of the first three bins are colored brown, olive, and pale green, respectively, in this histogram. The rightmost column in the data list shows the misfit angles, where the same coloring is used for the backgrounds of the angles smaller than 30°.

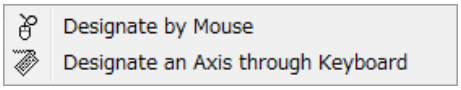


Figure 12: Submenu items of Misfit Angles.

radio-button ⊙ in the yellow panel indicates which of the stress axis $\sigma_1$ or $\sigma_3$ is chosen.

After a principal orientation is designated, the post processor enters the second mode to receive another principal orientation. In the second mode, an open circle glides along the great circle arc with the pole, the orientation of which has been designated through the first step, above. Click the left mouse button on the interested cluster to designate the principal orientation. Then, then the program enters the third mode to receive the stress ratio.

A Φ value is designated by one of the two ways. If the user specify one of the values 0.0, 0.1, 0.2,. . . , 0.9

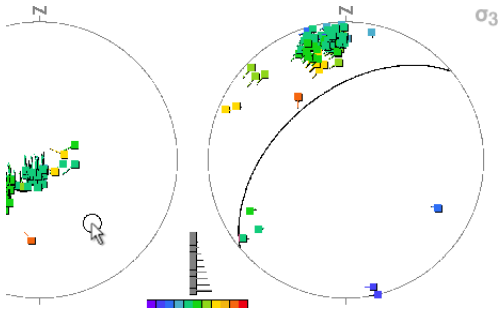


Figure 13: Screen-shot of the main window on which a state of stress is designated to calculate the misfit angles on the faults listed in the data window.

or 1.0, click one of the color blocks in the upper part of the main window (Fig. 15). A more precise value can be input through the box “B” in Fig. 15.

As soon as the designation of a state of stress is completed, the post processor calculates the theoreti-

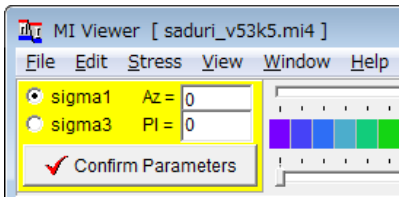


Figure 14: A principal orientation can be designated from keyboard using this panel.

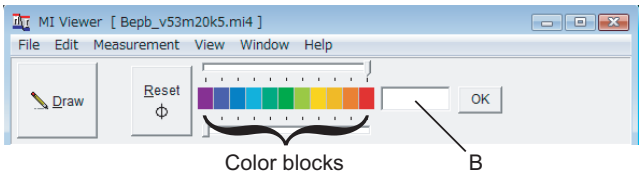


Figure 15: Upper part of the main window in the third mode to designate a state of stress.

cal slip directions of the faults, and plot the directions on the stereonet in the data window (Fig. 11). At the same time the program calculates the angular misfits between the theoretical and observed slip directions. The misfit angle of each fault is shown in the right-most column in the data list. The histogram in the same window shows the frequency of the misfit angles with the bin width of 10°. The program paints the first three bins brown, olive and pale green. The same color scheme is applied to the background of the right most column of the data list and to the symbols representing faults.

Contents of the stereonet and histogram can be saved in enhanced metafiles. The angular misfits shown in the table can be also saved in a text file. Use the pop-up menu shown in Fig. 9 for those purposes.


Figure 16: Paired stereograms showing two stress states, whose angular stress distance is shown in Fig. 17.

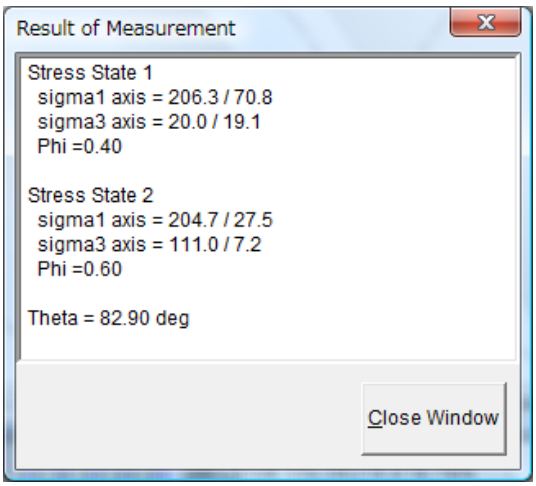


Figure 17: Angular stress distance (Θ) between Stress States 1 and 2, which are shown in Fig. 16.

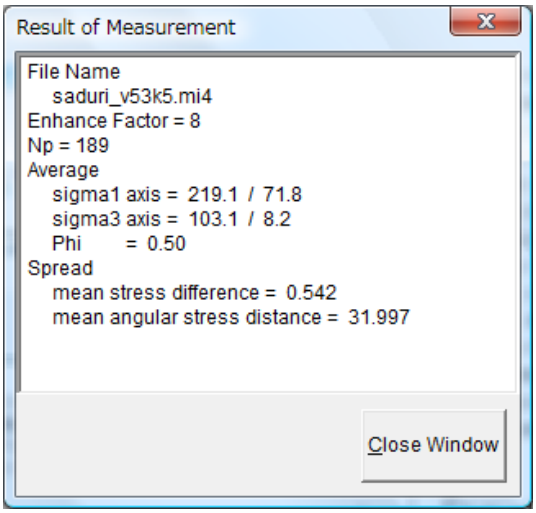


Figure 18: Dialog box showing statistical parameters of the stress states plotted as the tadpole symbols on the paired stereograms.

**[Angular Stress Distance]** The post processor has the function to calculate the difference between stress states (e.g., Fig. 16). Choose this menu item for this purpose. Then, the post processor calculates "angular stress distance" to measure this difference (Appendix B.5). Each of the stress states are input through the same procedure as that for calculating misfit angles. Fig. 17 shows the dialog window for indicating the angular stress distance between designated stresses (Fig. 16).

**[Global Average and Spread]** Choosing this menu item cues the program in calculating the averaged

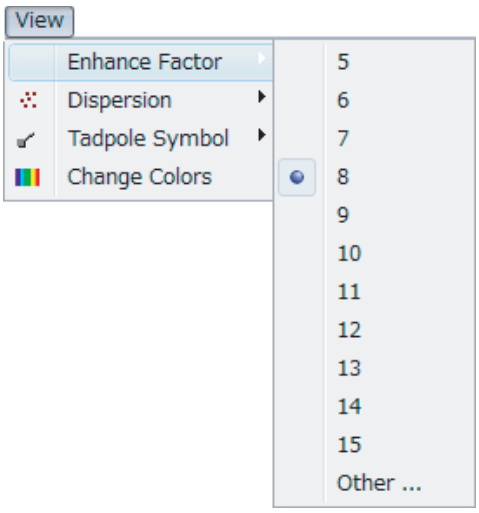


Figure 19: Enhance factor $e$ can be changed through this menu.

stress state and the spread around the average for *all* the stress states plotted on the paired stereograms in the main window[8]. These parameters are shown in a dialog box. The values 219.1 and 71.8 in Fig. 18 indicate the azimuth and plunge of the $\sigma_1$-axis of the average state of stress. The row sigma3 axis = ... indicates the $\sigma_3$-axis of this stress. The spread is denoted in two ways using mean stress difference, $\overline{D}$, mean angular stress distance, $\overline{\Theta}$. The definitions of the average and spread is given in Appendix B.6.

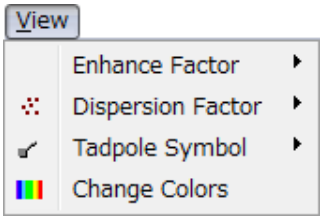


### 5.3.4 View menu

**[Enhance Factor]** On the paired stereograms in the main window, a great number of tadpole symbols are plotted. Clusters of the symbols represent significant stresses for given fault-slip data, but too many symbols makes it difficult for the user to take in the clusters. Namely, the clusters are obliterated by the noisy background in the stereograms. In that case, the user can thin out the background and, as a result, enhance the clusters. MI Viewer has this menu item for this purpose. The mechanism of thinning out the background is as follows.

The software package uses the computational grid points in the parameter space, each of which a state of stress. The number of grid points is $N_{\mathrm{G}} = 60{,}000$: we have the same number of stress states standing for any stresses. The multiple inverse method calculate a great number of stresses, and the stresses are approximated by the 60,000 stress states.

Let $m^{(i)}$ be the number of stresses stood for by the $i$th grid point. The post processor plots a number of $m^{(i)}/\max(es, 1)$ tadpole symbols on the paired stereograms, where $e$ is the enhance factor that the user specifies through the menu item Enhance Factor, $s$ the standard deviation defined by

$$s^2 = \frac{1}{N_{\mathrm{G}} - 1} \sum_{i=1}^{N_{\mathrm{G}}} \left[ m^{(i)} - \overline{m} \right]^2$$

and

$$\overline{m} = \frac{1}{N_{\mathrm{G}}} \left[ m^{(1)} + \cdots + m^{(N_{\mathrm{G}})} \right].$$

The default value of $e$ is 8; the program accepts integers in the range $0 \le e \le 99$. The user can choose the integers from the menu item shown in Fig. 19. The standard deviation is shown in the middle of the status bar with the prefix Sd (Fig. 4). Since the denominator of the fraction $m^{(i)}/\max(es, 1)$ is greater than or equal to the unity, this fraction is smaller or equal to $m^{(i)}$. Accordingly, the tadpole symbols are thinned out by this division to enhance clusters[9]. The total number of tadpoles plotted on each stereograms is

$$N_{\mathrm{p}} = \frac{m^{(1)} + \cdots + m^{(N_{\mathrm{G}})}}{\max(es, 1)}.$$

The left most section in the status bar shows three numbers, $N_{\mathrm{p}}$, number of grid points with $m^{(i)} > 0$ and $N_{\mathrm{G}}$, which are separated by slashes (Fig. 4).

To cancel this thinning out effect, set the value $e = 0$ through the submenu item Other...

**[Dispersion Factor]** It is not easy to see each tadpole symbols in a high density cluster, because the

[8]The next major revision of MI Viewer incorporates the function of clustering, which evaluates the average and spread of each cluster [27].

[9]This enhancing technique is simple, but the fact is that it spoils the resolution of the multiple inverse method. The clusters should be identified without the thinning with the enhance factor. For this purpose, it is necessary to find out clusters in the parameter space. We have tested some techniques [27]. A future version of this software suite shall implement artificial intelligence techniques for clustering in a high dimensional parameter space.

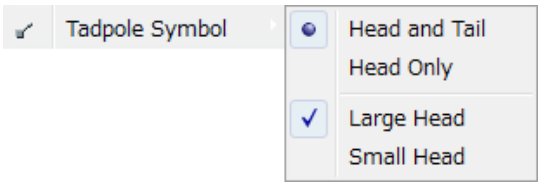


Figure 20: Attributes of the tadpole symbols.

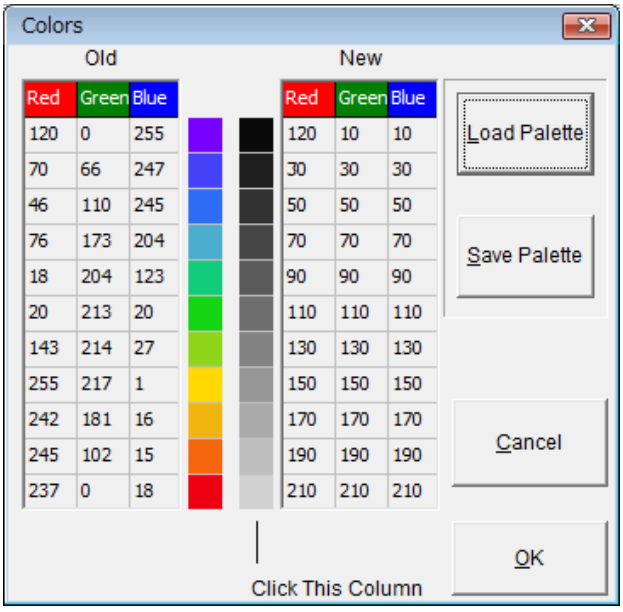


Figure 21: The color scheme to indicate stress ratios can be changed through this dialogue.

symbols lie one above another. In that case, the cluster can be dispersed by choosing a larger "dispersion factor" through this menu item. If it is set at zero, the symbols are plotted just at the points on the stereograms corresponding to the computational grid points.

**[Tadpole Symbol]** Other than colors, the tadpole symbols have several attributes. The tails help users to see the correspondence between the clusters in the left and right stereograms, but the tails are not necessary in some purposes. The submenu items Head and Tail and Head Only determine whether tails are plotted.

The heads have two sizes, large and small. Large ones may look nice for publication purposes. These options can be chosen from the submenu items Large Head and Small Head (Fig. 20).

**[Change colors]** The color scheme for distinguishing $\Phi$ values can be changed through this menu item. By choosing this, the dialog in Fig. 21 appears to show color palettes. This software package includes the three palette files, `rainbow0.pal`, `rainbow1.pal`, and `grayscale.pal`, in which different color schemes are recorded. The default color scheme is stored in the file `rainbow0.pal`. The user can load a palette file by clicking the Load Palette button.

The colors are indicated by their RGB values between 0 and 255 in the dialog shown in Fig. 21. There are two color columns in the dialog box. The left and right ones show the old and new color palettes, respectively. Click on a color box in the right column to change the color. The user can save his or her favorite color scheme in a text file with the extension `pal` by clicking the Save Palette button. The RGB values of the colors are expressed by hexadecimal values in the file.

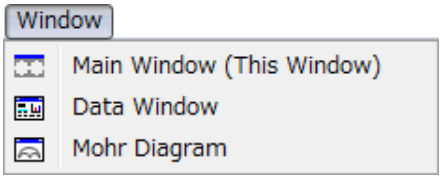


### 5.3.5 Window menu

This menu item prompts the user to select which window is activated. When the main window is hidden by the data window or other windows of MI Viewer, the main and data windows can be activated typing Alt + W on the keyboard.

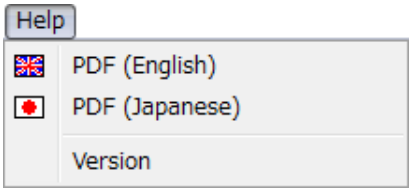


### 5.3.6 Help menu

There are three items in the Help menu. Choosing the first one opens this PDF file. The second one opens the user's manual in Japanese. The third item is to show the version number of the post processor.

## 5.4 Numerical experiments

The post processor has functions for simple numerical experiments needed to detect significant stress(es) from fault-slip data and to infer the correspondence between stress(es) and data. Once the post processor loads a datafile, the simulation is started by clicking

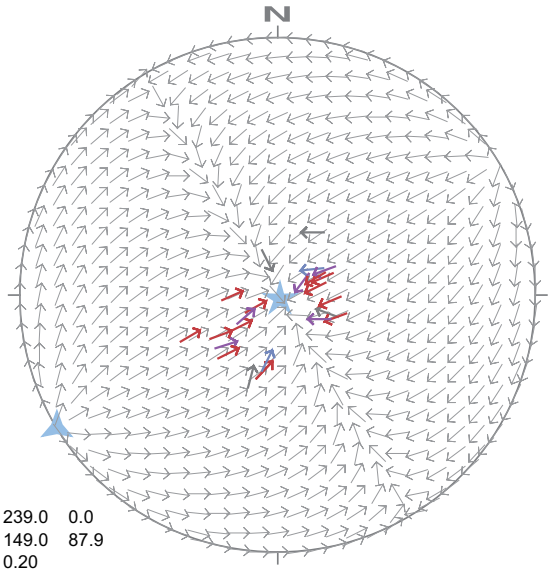


Figure 22: Tangent-lineation diagram showing the theoretical slip directions (thin gray arrows) for the state of stress whose parameters are shown at the lower left of this stereogram. The symbols ▲ and ★ denote the $\sigma_1$- and $\sigma_3$-axes, respectively. Thick arrows correspond to the fault-slip data in Fig. 11.

the menu item Misfit Angles. Fig. 11 shows one of the results of the simulation.

The experiments show the responses of the faults, the attitudes of which are shown in the data window, to various stress states. If the user specify a state of stress by the procedure explained in §5.3.3, MI Viewer calculates

- the theoretical slip direction
- misfit angle
- normal and shear stresses

of each fault (Appendix B.1).

The results are shown in the data window and in a Mohr diagram. Green dots in Fig. 11 indicate the theoretical slip directions for the state of stress with the parameters shown at the lower left of the stereogram in the window. At the same time values of misfit angles are shown in the rightmost column of the data list in the window. The background colors of this column indicate the ranges of misfit angles: 0–10°, 10–20°, 20–30° and > 30°. Fault-slip data are also plotted with these colors (Figs. 11 and 22). The misfit angles show which data are explained by the specified stress state.

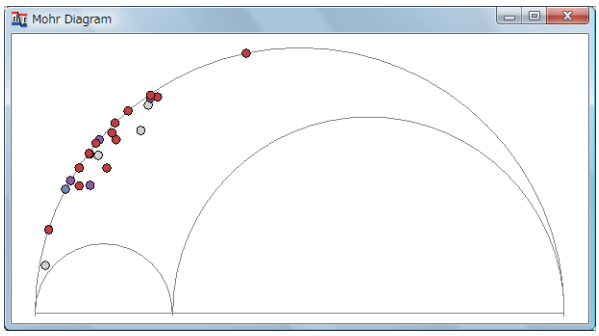


Figure 23: As soon as a state of stress is specified on the main window, the normal and shear stresses on the faults that are listed on the data window are calculated and plotted on a Mohr diagram.

The data in Fig. 11 are replotted as thick arrows in tangent-lineation diagram in Fig. 22. Colors of the arrows are the same wit the color scheme for misfit angles explained above. Thin gray arrows in the diagram denote the theoretical slip directions of faults with various attitudes. If the thick arrows are parallel to nearby thin arrows, the data represented by the thick arrows are explained by the specified stress.

The histogram of misfit angles is also shown under the stereogram. The 24 data in Fig. 11 are so nearly homogeneous that their optimal state of stress results in small misfit angles: 19 faults had misfit angles smaller than 20°. If there are a significant number faults with large misfit angles, at least a part of the data are incompatible with the specified stress.

Normal and shear stresses on the faults, the data of which MI Viewer has loaded, are calculated with the misfit angles, and plotted on a Mohr diagram (Fig. 23). Those quantities are normalized by the differential stress $\sigma_1 - \sigma_3$. If a row of the data list in the data window is clicked, the corresponding data point on the Mohr diagram is highlighted. The normal and shear stresses of the highlighted data are indicated on the right-hand side of Switch off Highlighting button (Fig. 11).

The results of the experiments can be stored in files through the pup-up window (Fig. 9). The contents plotted on the diagram can be stored by right-clicking on the diagram as well: the plot is saved as an enhanced metafile, and the normal and shear stresses are written in a text file (Fig. 24). Each row in the file has two items, i.e., normal and shear stresses.

| $\sigma_N$ | $\sigma_S$ |
|---|---|
| 0.122 | 0.327 |
| 0.151 | 0.297 |
| 0.226 | 0.403 |
| | 0.297 |
| ⋮ | |
| 0.148 | |
| 0.175 | 0.379 |
| 0.114 | 0.316 |

Figure 24: The normal and shear stresses, $\sigma_N$ and $\sigma_S$, plotted on the Mohr diagram (Fig. 23) are stored in a text file by right-clicking on the diagram. Those are normalized by the differential stress. Therefore, the normal stresses have values between 0 and 1; and the shear stresses between 0 and 1/2.

# 6 Preparing data files

The stress tensor inversion makes use of the attitudes of fault planes and the slip directions of hanging-walls to determine the stresses that can explain those pieces of information. The main processor reads two classes of data, geological fault-slip data and seismological focal mechanism data. Data of both classes are contained in text files with the file extension `fdt`. Orientations and directions are measured in degrees. Make a data file with a text editor, word processor, spreadsheet or other programs.

## 6.1 Fault-slip data

In a data file that contains fault-slip data from faults found at outcrops and borehole cores, etc., the parameters of one datum occupies a line (Fig. 25). And, the parameters must be written in the "FDT" format as follows. We refer data files with this format as FDT files.

The parameters of a fault-slip datum consists of the orientation of the fault plane and the slip direction of the hanging-wall block. We use the dip direction and the dip of the plane, $f_{az}$ and $f_{pl}$, to denote this orientation (Fig. 26). The slip direction is denoted by the orientation of slickenside striation and the sense of movement. The former is indicated by the azimuth of plunge of the striation, $s_{az}$ and $s_{pl}$. The latter is represented by the first letter of "Normal," "Reverse," "Dextral" and "Sinistral." The lower-case letters of the initials are acceptable. Fig. 25 shows fault-slip data in the FDT format. Blank lines are not acceptable. The angles are thought to be in the ranges, $0^\circ \le f_{az}, s_{az} < 360^\circ$ and $0^\circ \le f_{pl}, s_{pl} < 00^\circ$.

The main processor neglects any words or characters after the fifth item in a line (Fig. 25), so that the columns the character indicating the shear sense can be used for remarks.

(a)

| | | | | | |
|---|---|---|---|---|---|
| 152.0 | 82.0 | 63.1 | 8.0 | D ↲ | ① |
| 126.0 | 82.0 | 212.4 | 24.0 | S ↲ | ② |
| 315.0 | 73.0 | 4.0 | 65.0 | N ↲ | ③ |
| 298.0 | 59.0 | 335.0 | 53.0 | N ↲ | ④ |
| 295.0 | 50.0 | 296.6 | 50.0 | N ↲ | ⑤ |
| 303.0 | 51.0 | 307.8 | 50.9 | N ↲ | ⑥ |
| 299.0 | 50.0 | 309.8 | 49.5 | N ↲ | ⑦ |
| 293.0 | 49.0 | 296.0 | 49.0 | N ↲ | ⑧ |
| 304.0 | 47.0 | 297.0 | 46.8 | N ↲ | ⑨ |
| 310.0 | 44.0 | 288.0 | 41.8 | N ↲ | ⑩ |
| 295.0 | 61.0 | 210.6 | 10.0 | D ↲ | ⑪ |
| 299.0 | 47.0 | 307.8 | 46.7 | N ↲ | ⑫ |
| 331.0 | 82.0 | 44.4 | 63.8 | N ↲ | ⑬ |
| 121.0 | 83.0 | 210.8 | 2.0 | D ↲ | ⑭ |
| $f_{az}$ | $f_{pl}$ | $s_{az}$ | $s_{pl}$ | sense | |

(b)

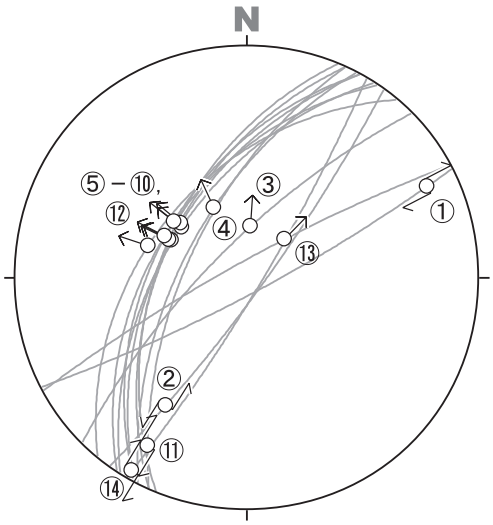


Figure 25: (a) Example of a data file. (b) Fault-slip data listed in (a). Lower-hemisphere, equal-angle projection. Numbers in open circles indicate the line numbers in the list.

It is recommended to check your data file with the stereonet software "SFSA." The SFSA is available from the software archive that includes this software package. SFSA loads data files with the FDT format, and visualizes their contents with a stereonet. The stereoplot can be exported to a metafile, which can be processed or decorated with drawing software such as Illustrator and Canvas. Fig. 25(b) was made through the procedure.

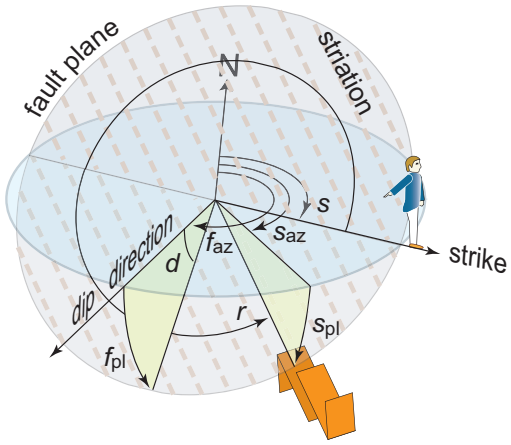


Figure 26: Schematic illustration showing the angles for indicating the orientation of a fault plane and the slip direction of the fault. The FDT format uses the four angles, $f_{az}$, $f_{pl}$, $s_{az}$ and $s_{pl}$, where $f_{az}$ is the dip direction, $f_{pl}$ equals the dip of the plane, and $s_{az}$ and $s_{pl}$ denote the azimuth and plunge of the striation. The strike $s$ and dip $d$ of the plane and the rake $r$ of the slip direction of the hanging wall are cataloged in focal mechanism data. The strike direction is defined by the "right-hand rule" [6]. The $r$ value of this example is in the range from 270° to 360°, because the fault has normal and sinistral senses.

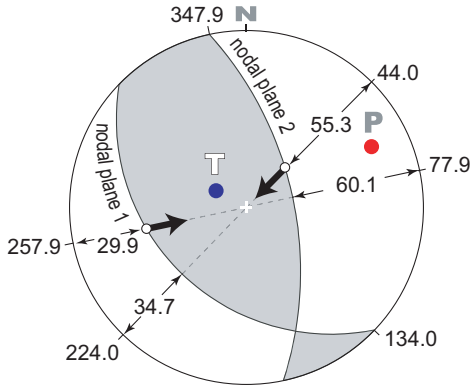


Figure 27: Lower-hemisphere, equal-angle projection showing a focal mechanism with nodal planes have the strikes, 134.0° and 347.9°, which are measured with the right-hand rule (Fig. 26).

## 6.2 Focal mechanism data

The difficulty of dealing with focal mechanism data for the stress tensor inversion is that it is not straightforward which of the nodal planes represents the fault surface that gave rise to the earthquake event (Fig. 27). First, we hypothesize that both the nodal planes acted as fault planes [30]. Then, we distinguish the nodal plane on which faulting occurred more probably than another for each mechanism using the post processor using the procedure in §7.

In a data file, parameters of a mechanism occupies two successive lines, each of which denotes the parameters of possible faulting on a nodal plane in the FDT format. For example, the mechanism illustrated in Fig. 27 has the hypothetical fault-slip data:

```
224.0  34.7  257.9  29.9  R
 77.9  60.1   44.0  55.3  R
```

The first and second lines correspond to the southwestward and eastward dipping nodal planes, respectively.

However, the FDT format is not used in the catalogs of focal mechanisms that are provided by seismological institutes. Instead, the rake $r$ of the hanging-wall's slip direction is usually recorded along with the strike $s$ and dip $d$ of each nodal plane (Fig. 26). Given such data, those angles should be transformed to the equivalent parameters in the FDT format for our stress inversion software.

For this purpose, the program, `rake2fdt.exe`, is included in this software package (Fig. 28). To do so, prepare a text file containing focal mechanisms expressed in terms of the angles such that

```
134.0   34.7   61.1  ↵
347.9   60.1  108.5  ↵
```

These successive lines represent the mechanism in Fig. 27. Entries in each line are separated by one or more spaces, and "↵" denotes the newline code. The program, `rake2fdt.exe`, reads a data file in the *s*-*d*-*r* format, and output a corresponding FDT file (Fig. 28). The file `sample_R2FDT.txt` in this package is a sample file of this program.

In conclusion, follow the procedure:

1. Make a text file containing focal mechanisms. Each mechanism is described in successive two lines with the data format as the list in the blue box above. Each line has the $s$, $d$, and $r$ values of a nodal plane.

2. Convert this data format to the FDT format through `rake2fdt.exe`. The resultant FDT file must have the file extension `fdt`.

The main processor input this file, and apply an algorithm for focal mechanisms.

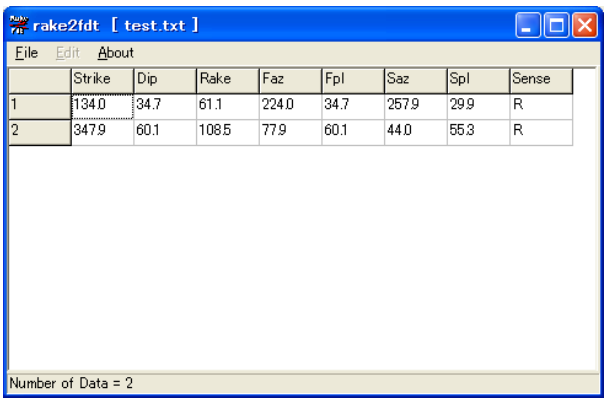


Figure 28: The software tool, `rake2fdt.exe`, for format conversion.

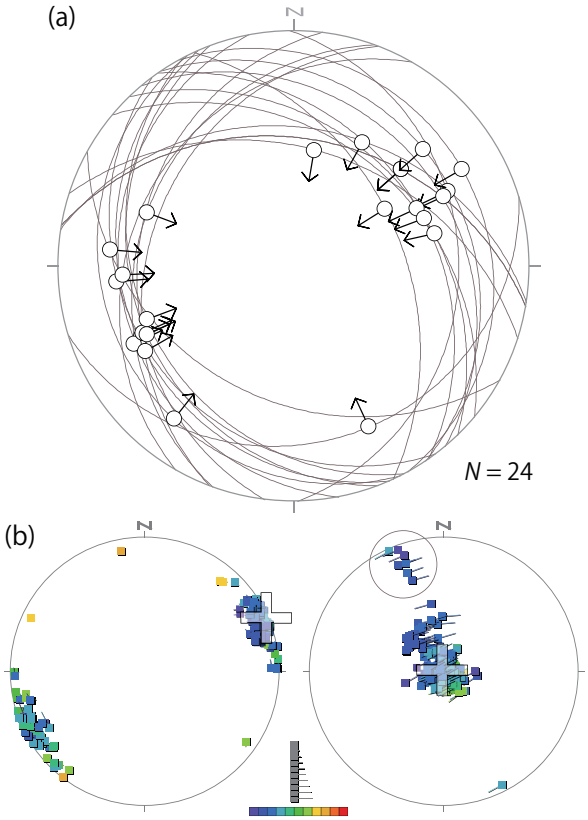


Figure 29: (a) Nearly homogeneous fault-slip data. Lower-hemisphere, equal-angle projection. (b) Result of the multiple inverse method (ver. 6) applied to the data in (a) with the parameters, $k = 5$ and $e = 8$. Crosses indicate the principal orientations of the optimal stress for the data. The optimal solution has the stress ratio at 0.26.

# 7 Worked problems

## 7.1 Homogeneous data

The present method was made for dealing with heterogeneous datasets, but can determine the optimal stresses from homogeneous ones as well.

The 24 fault-slip data in Fig. 29a are used to illustrate the processing of homogeneous data with noises. This dataset is composed of NE and SW dipping thrust faults with a few exceptions. So, the faults seem to be a mixture of a conjugate set and a few faults with other origin, meaning that the dataset is somewhat heterogeneous. We regard the exceptional as noises added to a homogeneous dataset. The problem we are solving, here, is the procedure of how the optimal stress is obtained from such a dataset and how the precision of the solution is estimated.

Fig. 29b shows the result of the present method applied to the 24 data. Since the data are not literally homogeneous, tadpole symbols with various colors from violet to yellow make clusters with the radii of ~20°.

The optimal stress for the dataset is obtained from the dialog window opened by clicking Global Average and Spread under Measurement menu of MI Viewer. The dialog says the principal orientations and stress ratio of the optimal state of stress of the dataset. The orientations are illustrated in Fig. 29b. In addition, the dialog says that $\overline{\Theta} = 20.6°$, similar to the radii of the clusters in the figure. $\overline{\Theta}$ is a measure for indicating the precision of the solution [49]. Fig. 44 illustrates relationship between the spread of clusters in the main window and noise levels of data.

Green dots in Fig. 30a show the theoretical slip directions of the faults. Let us regard a fault-slip datum with the misfit $< 20°$ as being compatible with the state of stress from which the misfit angle was calculated. Fig. 30a shows that nineteen faults are explained by the optimal stress but five faults are not. This classification of faults may be a clue to understand the spatial and/or temporal variations of stress in the study area. If the five data are not noises but have geological significance, the optimal stress for those should be further determined. Fig. 30b shows the optimal stress for the five data.

There is a cluster of blue tadpoles encircled in Fig. 29b. Mohr diagrams for the 24 data drawn with the stresses indicated by the crosses and those tadpoles are shown in Fig. 31a. Almost all data points are plotted along the inner Mohr circle that has the diameter between $\sigma_2$ and $\sigma_1$ along the abscissa, indicating that the stress was unfavorable for the faults but they were activated by small shear stresses. The $\sigma_3$ axis is subparallel to many fault planes (Fig. 29), resulting in the small shear stresses. In contrast, the Mohr diagram

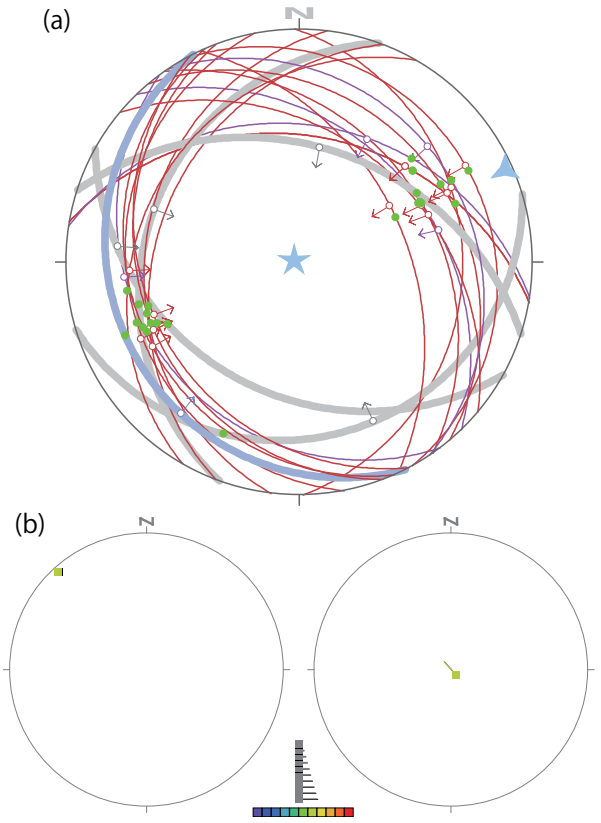


Figure 30: (a) Faults shown in Fig. 29a and their theoretical slip directions (green dots) under the optimal stress in Fig. 29b. Thick blue and gray lines show the attitudes of the faults with the misfit angles in the ranges 20–30° and > 30°, respectively. (b) The optimal stress for the five data which are depicted by thick lines in (a). This diagram was captured with the dispersion factor at zero.

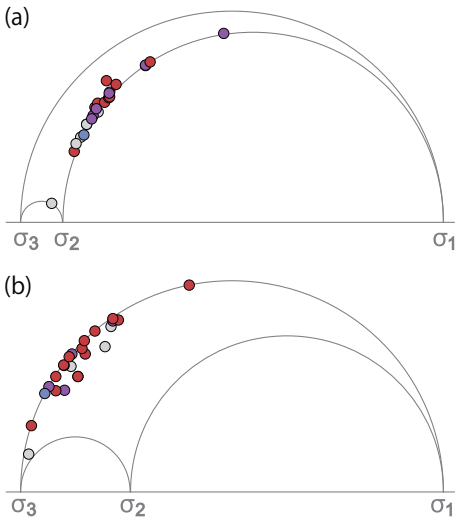


Figure 31: (a) Mohr diagram for the data drawn with the stress indicated by the cluster encircled in Fig. 29b. (b) Mohr diagram for the data in Fig. 29a drawn with the optimal solution indicated by the crosses in Fig. 29b. Colors of data points correspond to the ranges of misfit angles (p. 15).

drawn with the optimal stress indicated by crosses in 29b has data points almost along the outer Mohr circle connecting $\sigma_3$ and $\sigma_1$ (Fig. 31b). Therefore, it is natural that the optimal stress activated most of the faults, but it is not for the stress suggested by the small cluster. The encircled cluster improbably indicate the second significant stress. Instead, it is probably a part of the girdle made by blue tadpoles in the right stereogram in Fig. 29b: the color indicates so low a stress ratio that $\sigma_3$-axis is much more unstable than $\sigma_1$-axis of the optimal solution.

## 7.2 Heterogeneous data

The stress states compatible with data are represented by clusters in our method. It is important to consider the significance of the clusters. And, once they are determined to be significant, the sorting of faults or focal mechanisms, e.g., the correspondence between the stresses and data, is important as well. Both the identification of significant stresses and the grouping of faults according to those stresses use the misfit angles of faults. The angles are evaluated by the Wallace-Bott hypothesis (p. 23).

However, both results of those tasks include fuzziness to some extent, because the hypothesis is a week constraint for them. Specifically, different stress states can activate a fault in the same direction. Admitting this fuzziness, the tasks are done as follows.

Misfit angles, which can be obtained by MI Viewer, are the keys for the tasks. Let $d$ be this angle. The smaller the angle is, the higher the probability is for the fault to be activated by the stress that is assumed to calculate the misfit angle. For this purpose we use a threshold angle $d_T$. Fault-slip data with their $d$ values smaller than this threshold, the data are said to be compatible with the stress, or to be explained by the stress. Traditionally, the values from 15° to 30° were assigned to this threshold, so the misfit angles smaller than 30° is highlighted by colors in the data window (Fig. 5). We prefer 20° for the threshold value. For the case of the misfit angles in Fig. 5, the state of stress with the $\sigma_1$- and $\sigma_3$-axes in the orientations 110.7°/75.7° and 225.0°/6.0°, respectively, and $\Phi = 0.3$, 9 faults satisfy the condition $d < 20°$. Those faults are determined to have been activated probably

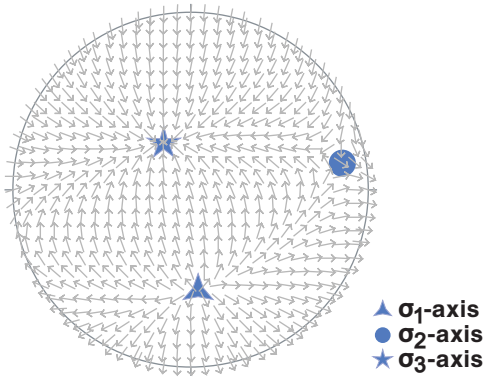


Figure 32: Tangent-lineation diagram showing the orthorhombic symmetry of the theoretical slip directions (gray arrows) for the state of stress with $\Phi = 0.5$ and the stress axes shown in this picture. Note that the directions rapidly changes around the principal orientations.

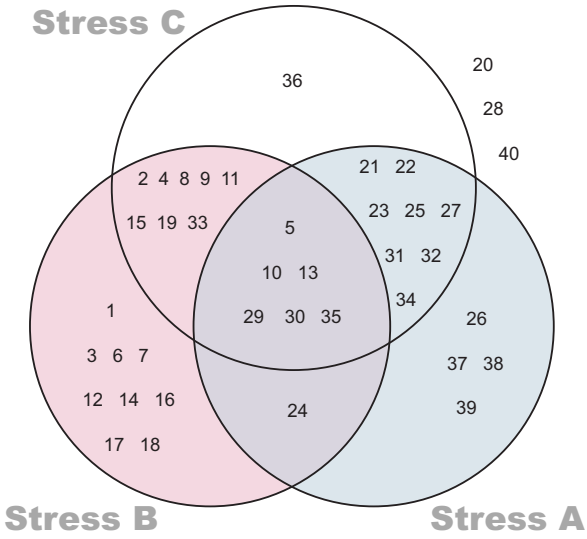


Figure 33: Venn diagram showing the compatibility of 40 fault-slip data with Stresses A, B, and C.

by this state of stress. Other faults were not.

However, it must be noted that the theoretical slip direction is unstable when the fault plane in question is approximately parallel to one of the stress axes. That is, the Wallace-Bott hypothesis predicts that both small perturbations in the fault attitude and/or the principal orientations of the stress give rise to a large change in the theoretical slip direction on the plane (Fig. 32). Every datum including the attitude of fault has measurement errors. Therefore, the misfit angles for those faults nearly parallel to one of the assumed stress axes have uncertainty. In addition, such a fault is difficult to be activated by the stress from which the unstable misfit angle is evaluated, because the shear stress acting on the fault plane is small. However, such a fault can be activated by the stress, provided that pore pressure is very large. To see whether a fault normal is nearly parallel to a stress axis, the tangent-lineation diagram on the data window is useful (Figs. 11 and 32).

## 7.3 Examples

Two examples are used in this subsection to explain how significant stresses are identified from heterogeneous data and how faults are classified using the identified stresses.

### 7.3.1 Example 1

The first example is the problem of identifying significant stresses from heterogeneous 40 fault-slip data. Suppose that there clusters appear in the paired stereograms corresponding to the Stresses A, B, and C. The Venn diagram in Fig. 33 schematically shows the compatibility of the 40 data with the three stresses. The diagram denotes, for example, that the 24th datum is compatible with Stress A and B but is not with Stress C; and that the 20th, 28th, and 40th data are compatible with none of the three stresses. Consequently, the three data are neglected in the argument below. The faults corresponding to them were nor activated by the stresses, or their misfit angles have little confidence levels.

First, the 36th datum is compatible only with Stress C, but Stresses A has many data that are explained only by Stress A. The same is true for Stress B. Consequently, Stress C is neglected by Óccam's rázor as an insignificant solution for the 40 data.

Next, we arrive at the problem of classifying data. As Stress C has been ignored, the data in the colored areas in Fig. 33 are examined. The data in the light blue area are thought to be activated by Stress A, and those in the pink area by Stress B. Those data have clear belongings. In contrast, those in the light violet area are fuzzy. Stresses A and B can explain the data.

### 7.3.2 Example 2

The separation of stresses from heterogeneous data is difficult if the numbers of data corresponding to the stresses have large differences. Example 2 is devoted to explain the way to deal with those data.

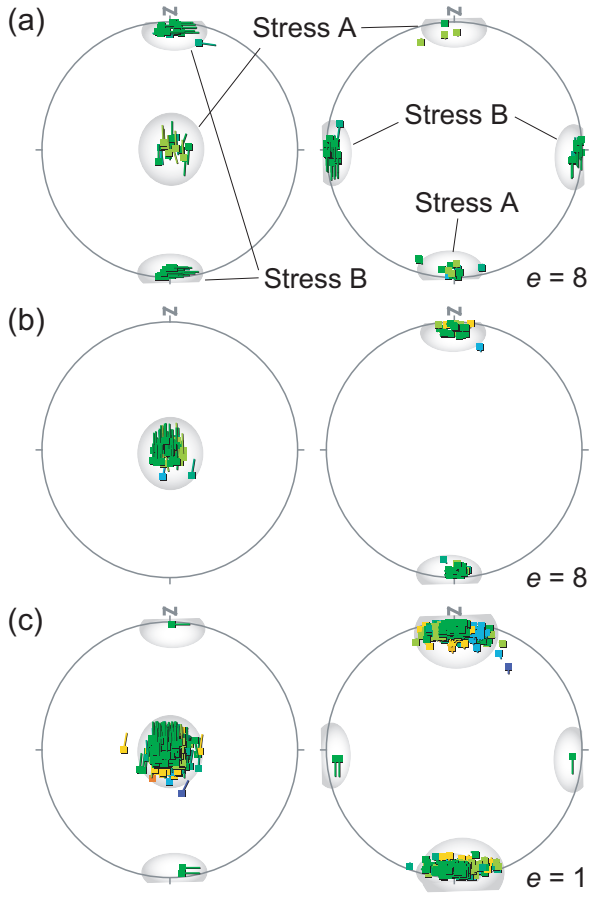


Figure 34: (a) Result of the multiple inverse method applied to 60 fault-slip data: Both Stresses A and B are assumed to activated 30 faults. (b) Result for the case of the numbers of faults were 30 and 10, respectively. (c) Same with (b) but a different value of enhance factor $e$.

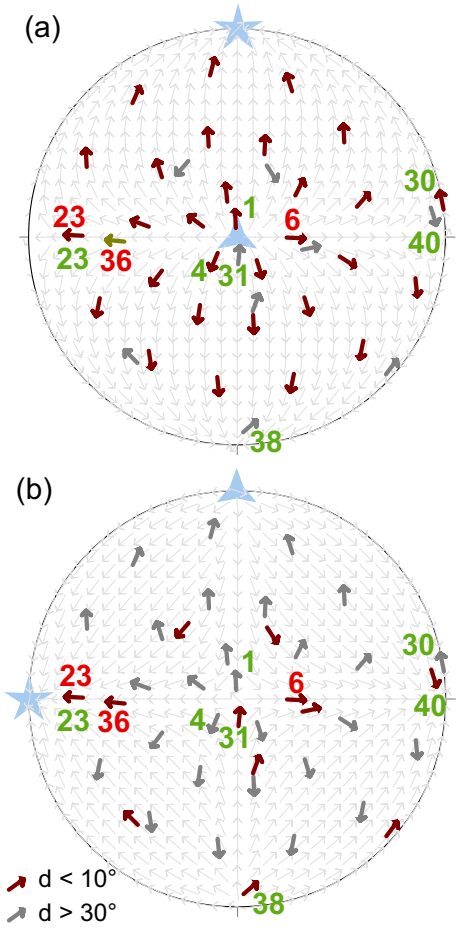


Figure 35: Tangent-lineation diagrams showing the theoretical slip directions for Stress A (a) and Stress (b) in Fig. 34. Values of the angles are listed in Table 2. Thick arrows indicate those of the 40 faults in Table 2. The $\sigma_1$ and $\sigma_3$ orientations indicated by the symbols ▲ and ★, respectively. Note that Faults numbered 6, 23, and 36 move nearly the same directions under the stresses.

Suppose that Stress states A and B activated $N_A$ and $N_B$ faults. Fig. 34(a) shows that the multiple inverse method can easily separate the stresses if $N_A \approx N_B$, though the difficulty comes also from the similarity of the stresses. Both the stresses are assumed to have the $\Phi$ values at 0.5; Stress A is of the normal faulting regime with N–S extension, and Stress B is of the strike-slip faulting regime with E–W extension[10]. The two clusters corresponding to the stresses have roughly the same number of tadpole symbols in the paired stereogram (Fig. 34(a)).

The problem we are tackling here is the case that $N_A$ is a few times larger than $N_B$. Fig. 34(b) shows the case $N_A = 30$ and $N_B = 10$. Only Stress A makes a cluster in the paired stereogram when the enhance factor is at the default value of 8. However, when the enhance factor is 1, the cluster corresponding to Stress B appears as well (Fig. 34(c)). The small number of tadpole symbols in this cluster seems to suggest that this is a insignificant stress for the data, but this is decided to be incorrect as follows.

For this judge, we use the list of misfit angles such as Table 2.The items with brown backgrounds in this list have misfit angles smaller than $d_T = 20°$. It is obvious from this table that Stress A does not explain the data number from 30 through 40 with one exception (the 36th datum). Although Stress B was depicted by a thin cluster in Fig. 34(c), the stress explains 12 data, 30% of the total number of data. Accordingly, Stress B is found to be essential and significant for the data.

[10]The normal, strike-slip, and reverse faulting regimes of stress have nearly vertical $\sigma_1$-, $\sigma_2$-, and $\sigma_3$-axes, respectively.

Table 2: The misfit angles of 40 data for Stresses A and B in Fig. 34. The angles smaller than $d_T < 20°$ have brown backgrounds. Items in gray columns denote datum numbers of fault-slip data.

| | A | B | | A | B |
|---|---|---|---|---|---|
| 1 | 0.0 | 171.3 | 21 | 0.1 | 151.7 |
| 2 | 0.0 | 157.5 | 22 | 0.0 | 142.0 |
| 3 | 0.1 | 62.6 | 23 | 0.1 | 7.5 |
| 4 | 0.1 | 112.7 | 24 | 0.0 | 127.8 |
| 5 | 0.1 | 126.0 | 25 | 0.0 | 138.3 |
| 6 | 0.1 | 3.2 | 26 | 0.1 | 152.2 |
| 7 | 0.0 | 105.8 | 27 | 0.0 | 139.7 |
| 8 | 0.0 | 146.9 | 28 | 0.1 | 146.9 |
| 9 | 0.0 | 146.5 | 29 | 0.1 | 143.9 |
| 10 | 0.1 | 115.2 | 30 | 0.1 | 178.4 |
| 11 | 0.0 | 36.1 | 31 | 171.3 | 0.1 |
| 12 | 0.1 | 89.2 | 32 | 152.4 | 0.0 |
| 13 | 0.0 | 135.4 | 33 | 31.3 | 0.1 |
| 14 | 0.0 | 158.6 | 34 | 134.1 | 0.1 |
| 15 | 0.0 | 117.1 | 35 | 123.0 | 0.1 |
| 16 | 0.0 | 61.2 | 36 | 11.0 | 0.1 |
| 17 | 0.1 | 86.6 | 37 | 142.6 | 0.1 |
| 18 | 0.1 | 135.4 | 38 | 144.2 | 0.2 |
| 19 | 0.0 | 141.1 | 39 | 174.3 | 0.0 |
| 20 | 0.2 | 143.5 | 40 | 138.5 | 0.1 |

In this list, the data number 6, 23, and 26 are compatible with the both stresses. The faults corresponding to the data are activated almost the same directions by Stresses A and B. Therefore, they are explained by the both stresses.

It should be also noted that 7 fault planes among the 40 ones have the poles nearly perpendicular to one of the assumed stress axes. The green letters in Fig. 35 shows the datum numbers in Table 2 with the fault planes and its poles making angles less than 20° with the axes. The misfit angles themselves of those faults are less confident than others.

Without those data of which datum numbers are denoted by green or red letters in Fig. 35, the fault classification according to the detected stresses is complete. The belongings of those data are fuzzy.

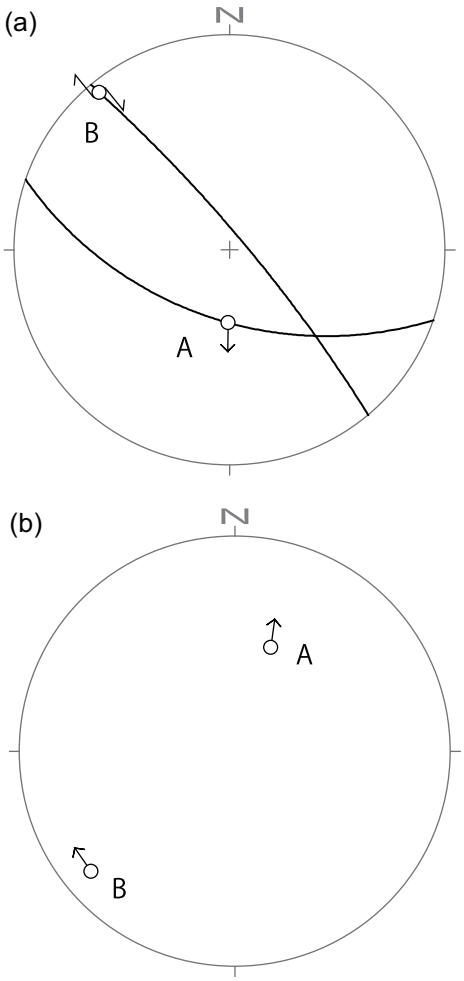


Figure 36: Two methods for visualizing fault-slip data. Lower-hemisphere, equal-angle projections. Attitudes of the faults A and B are denoted by great-circles (a) and poles (b). The latter method is called a tangent-lineation diagram [38].

# Appendices

## A Plotting methods of fault-slip data

Two plotting methods are used in this software package. Stereograms in Fig. 36 illustrate them with the same data. The first one exhibits the attitudes of faults by great-circles (Fig. 36a). And, the slip directions of hangingwall blocks are indicated by arrows attached to the great-circles. That is, reverse and normal faults are denoted by arrows pointing at the center of stereogram and by those with opposite directions, respectively. Strike-slip faults are exhibited by paired ar-

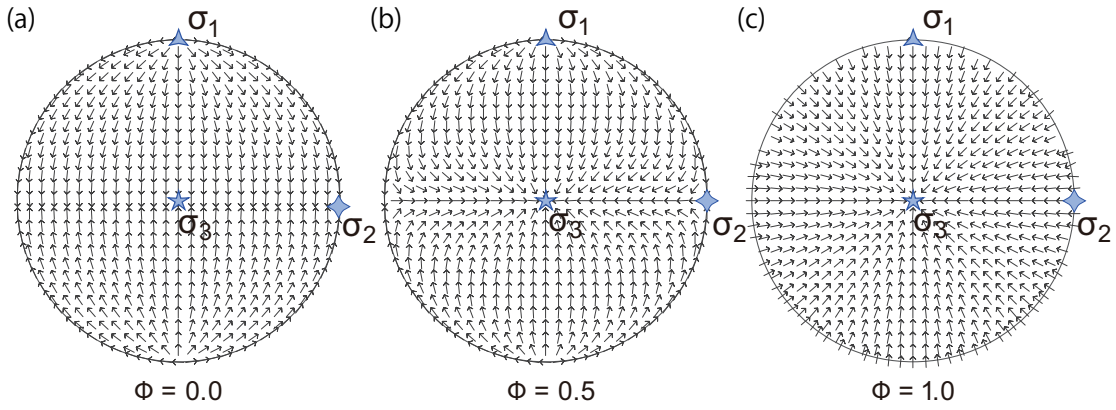


Figure 37: Tangent-lineation diagrams for three stress states that have the same principal orientations but different stress ratios. Lower-hemisphere, equal-angle projections. Note the symmetry of the patterns made by arrows.

rows attached on the great-circles. If the arrows are drawn in a clockwise manner as those of the fault B in Fig. 36a, the fault has a dextral sense of movement. Those in a counterclockwise manner indicate a sinistral sense of movement.

The plotting method illustrated in Fig. 36a straightforwardly shows fault-slip data, but is inconvenient for theoretical considerations. Tangent-lineation diagrams (Fig. 36b) are convenient for this purpose. In this diagram, a fault-slip datum is depicted by a small arrow in a stereogram. The arrow is plotted at the point indicating the pole to the fault plane. The arrow indicates the slip direction of the footwall block with respect to the hanging wall block. If the arrow is drawn adjacent to the great-circle that the horizontal plane, the fault has nearly vertical surface. And, if its arrow is subparallel to this great-circle, the arrow represents a strike-slip fault. Such an arrow with a clockwise sense with respect to the center of the stereogram indicates a dextral-sense of movement. Dip-slip faults are indicated by arrows pointing at the center of the stereogram or by those with opposite directions. The faults A and B in Fig. 36b are accordingly dextral strike-slip and normal faults, respectively.

The advantage of tangent-lineation diagrams is demonstrated in Fig. 37, which shows fault movements predicted by the Wallace-Bott hypothesis (Appendix B.1). If the patterns made by arrows in this figure are compared to those of streams, $\sigma_1$- and $\sigma_3$-orientations in the diagram denote the source-sink pair. Triaxial stresses ($0 < \Phi < 1$) have a saddle-point at the $\sigma_2$-orientation. The patterns reflect the symmetry of stress states. Triaxial stresses have orthorhombic symmetry, whereas stress states with $\Phi = 0$ or 1 have axial symmetry.

Therefore, if a homogeneous dataset is plotted on a tangent-lineation diagram, arrows make one of such patterns. And, the source an sink of the stream pattern indicate the $\sigma_1$- and $\sigma_3$-orientations. In other words, the determination of stress from a homogeneous dataset is equivalent with a problem of fitting such a pattern on the diagram.

# B Theories

The basics of stress tensor inversion, the basic idea and algorithms of the multiple inverse method are briefly explained in this appendix. The method is fully explained in the articles [29, 30, 46]. For the separation of stresses from heterogeneous data, we have developed not only software but also the basic theories of stress tensor inversion, which are explained in the articles [33, 34, 49]. We use the rectangular coordinates in Fig. 38. The knowledge on thie coordinates is needed only when the user reads the stress components downloaded from the post processor through the menu item Save Coordinates (p. 10).

## B.1 Wallace-Bott Hypothesis

The multiple inverse method evolved from the classical stress tensor inversion. These methods are based on the Wallace-Bott hypothesis, which relates stress with slip directions of faults [7, 43]. The stress denoted by the tensor $\boldsymbol{\sigma}$ results in the traction $\boldsymbol{t} = \boldsymbol{\sigma}\boldsymbol{n}$ on the fault plane that has the unit vector $\boldsymbol{n}$ perpendicular to the plane. In other words, the attitude of the fault is represented by this unit vector. The normal and shear

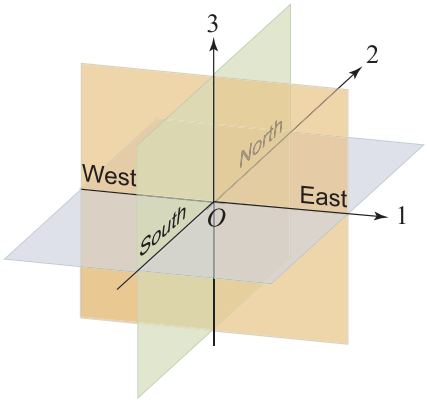


Figure 38: Rectangular Cartesian coordinates used in this software package.

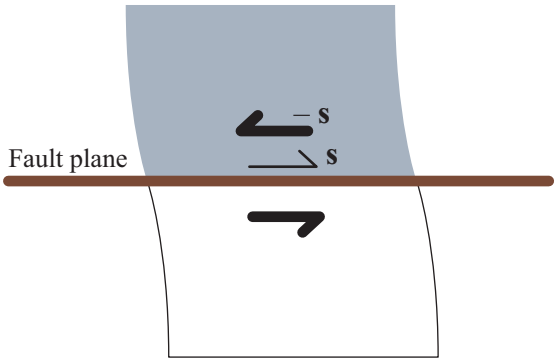


Figure 39: Schematic picture showing the senses of shear and fault movement. Thin arrow denotes the shear stress $\boldsymbol{s}$ acting on the hangingwall block by the footwall. Thick arrows indicate the sense of fault movement resulting from the shear stress. The movement of the hangingwall block is in the direction opposite to $\boldsymbol{s}$.

stresses acting on the plane are written as

$$\sigma_{\mathrm{N}} = \boldsymbol{t} \cdot \boldsymbol{n} \tag{2}$$

$$\sigma_{\mathrm{S}} = \left| \boldsymbol{t} - \sigma_{\mathrm{N}} \boldsymbol{n} \right| \tag{3}$$

When the post processor draws Mohr diagrams, normal and shear stresses are normalized by the differential stress. As a result, their values have the ranges 0–1 and 0–0.5, respectively.

The Wallace-Bott hypothesis says that faulting occurs in the direction parallel to the shear stress on the fault plane. Eq. (3) denotes magnitude of the shear stress, whereas the vector

$$\boldsymbol{s} = \boldsymbol{t} - \sigma_{\mathrm{N}} \boldsymbol{n} \tag{4}$$

denotes its magnitude and direction. Faulting occurs to relieve this shear stress. Therefore, the fault movement is indicated by $-\boldsymbol{s}$ rather than $\boldsymbol{s}$ (Fig. 39).

Once $\boldsymbol{\sigma}$ is assumed, the slip direction of faults with any orientations can be calculated through Eq. (4). And, we can calculate the misfit angles, $d$, between observed fault slip directions and the theoretical ones predicted by the hypothesis with an assumed $\boldsymbol{\sigma}$. If the observed and theoretical slip directions of a fault is denoted by the unit vectors $\boldsymbol{s}^{(\mathrm{obs})}$ and $\boldsymbol{s}^{(\mathrm{theory})}$, respectively, the equation,

$$d = \cos^{-1}\left[\boldsymbol{s}^{(\mathrm{obs})} \cdot \boldsymbol{s}^{(\mathrm{theory})}\right],$$

gives the misfit angle of this fault, where

$$\boldsymbol{s}^{(\mathrm{theory})} = -\boldsymbol{s}/|\boldsymbol{s}|. \tag{5}$$

Note that the denominator in Eq. (5) vanishes if the fault plane is perpendicular to one of the stress axes. In that case, the slip direction is indeterminable. This is depicted as three types of singular points, i.e., source, sink and saddle point, in tangent-lineation diagrams (Fig. 37). It is natural that the pattern made by $\boldsymbol{s}^{(\mathrm{theory})}$ inherits symmetry from the stress tensor. This is reflected by the symmetry in the diagrams.

## B.2 Stress states

A stress state is defined by a $\Phi$ value and principal orientations. Stresses with different principal stress values can be the same stress state, providing that they have a common $\Phi$ value and common principal orientations. Such stresses are collectively called the state of stress as well. For example, suppose the state of stress characterized by the E–W trending $\sigma_1$-axis and N–S trending $\sigma_3$-axis and $\Phi = 0.5$. This stress state includes the stresses with the combinations of the principal stresses not only {1 MPa, 2 MPa, 3 MPa} but also {30 MPa, 35 MPa, 40 MP}.

We use the above definition of stress states, because the Wallace-Bott hypothesis indicates that stresses included by a stress state result in the same slip directions. Stress tensor inversion methods including ours are based on the hypothesis to determine stresses from the observed slip directions of many faults. Therefore, the methods cannot determine the absolute values of principal stresses.

The fact that the absolute values cannot be determined by the methods has good and bad points. The indeterminacy itself is, of course, the bad point. However, thanks to the indeterminacy, we can estimate stress states from faults without worrying the paleo-

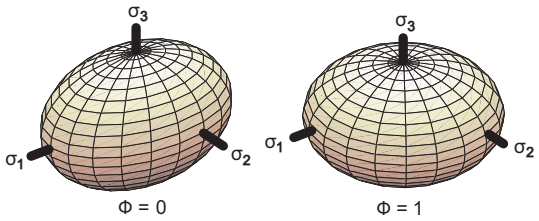


Figure 40: Stress ellipsoids for the stresses with the Φ values at 0 and 1. The ellipsoids have axial symmetry about the $\sigma_1$- and $\sigma_3$-axes, respectively.

depths of the faults nor the paleo-pore pressures of the times they moved. The paleo-depth and paleo pore pressures are difficult quantities for geological observations. Pore pressure is important for fault activity, but the pressure $p$ does not affect the Φ values. So, data from different portion of a rock mass with different pore pressures can be used to determine the state of stress in the mass. If linear elasticity is assumed for the crust, the principal stresses are proportional to depth, and the stress ration in the crust is independent from depth. Therefore, a stress state can be determined from data from different depths. If this proportionality is disturbed, and if depth zones have different stress states, the states can be estimated by the multiple inverse method using data from different depth zones.

An ellipsoid gives geometrical interpretation of a stress state. The ellipsoid representing the state of stress has the principal axes parallel to the principal stress axes and the principal radii, $a$, $b$, and $c$, satisfying that $(b-c)/(a-c)$ equals the Φ value of the stress state, where the inequality $0 < c \leq b \leq a$ is assumed. This figure coincides with the stress ellipsoid corresponding to the state of stress (Fig. 40), provided that all the principal stresses are positive in sign.

## B.3 Reduced stress tensors

Stresses are generally represented by $3 \times 3$ symmetrc matrices. A reduced stress tensor represents the stress tensors that have common principal orientations and the common Φ value.

We use the reduced stress tensors with defined by the equation [33],

$$\boldsymbol{\sigma} = \frac{1}{\Lambda}\boldsymbol{R}^{\top}\begin{pmatrix} 2-\Phi & 0 & 0 \\ 0 & 2\Phi-1 & 0 \\ 0 & 0 & -\Phi-1 \end{pmatrix}\boldsymbol{R}, \qquad (6)$$

because this type of reduced stress tensors have advantages. $\Lambda = \sqrt{3\Phi^2 - 3\Phi + 3}$ is the normalizing factor, and $\boldsymbol{R}$ is the orthogonal tensor representing the principal orientations. The advantages include not only the reduction of the stress inversion problems to geometrical problems [48] in the parameter space explained in Appendix B.4 but also the facility of defining distance between reduced stress tensors (Appendix B.5) and of evaluating the mean and its confidence level for a given set of reduced stress tensors (Appendix B.6). Reduced stress tensors of the type of Eq. (6) satisfy the conditions,

$$\sigma_1 + \sigma_2 + \sigma_3 = 0 \qquad (7)$$

$$\frac{1}{2}\left(\sigma_1^2 + \sigma_2^2 + \sigma_3^2\right) = 1. \qquad (8)$$

the left-hand sides of which are the first and second basic invariants of $\boldsymbol{\sigma}$. Components of a tensor change their values with coordinate rotations. That is, if the coordinate system different from that in Fig. 38 is chosen, the components of $\boldsymbol{\sigma}$ has different components from those defined by the coordinate system in the figure. Invariants of a tensor are the quantities characterizing the physical entity of the tensor, and are not affected by coordinate rotations.

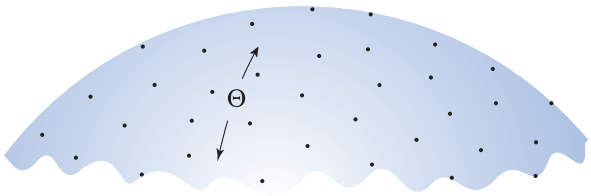


Figure 41: Schematic illustration showing the parameter space for representing stress states. The unit hypersphere in a five-dimensional Euclidean space is used as this space. Dots on the blue sphere indicate computational grid points on the hypersphere. Distance between stress states is defined by the angular distance, Θ, between the points on the hypersphere that represent the stress states.

## B.4 Parameter space

Stress states are represented by points in a parameter space in stress tensor inversion. The multiple inverse method replaced the naive parameter space, which was defined when the method was invented[11], with an advanced parameter space in 2005. The replacement

[11] The naive parameter space is the four-dimensional Euclidean space that is span by the rectangular Cartesian coordinates, $O$-$\theta\phi\psi\Phi$, where $90^\circ - \theta$ is the plunge of the $\sigma_3$-axis, $\phi$ the strike of the $\sigma_1\sigma_2$-principal stress plane, and $\psi$ the rake of $\sigma_1$-axis [46].

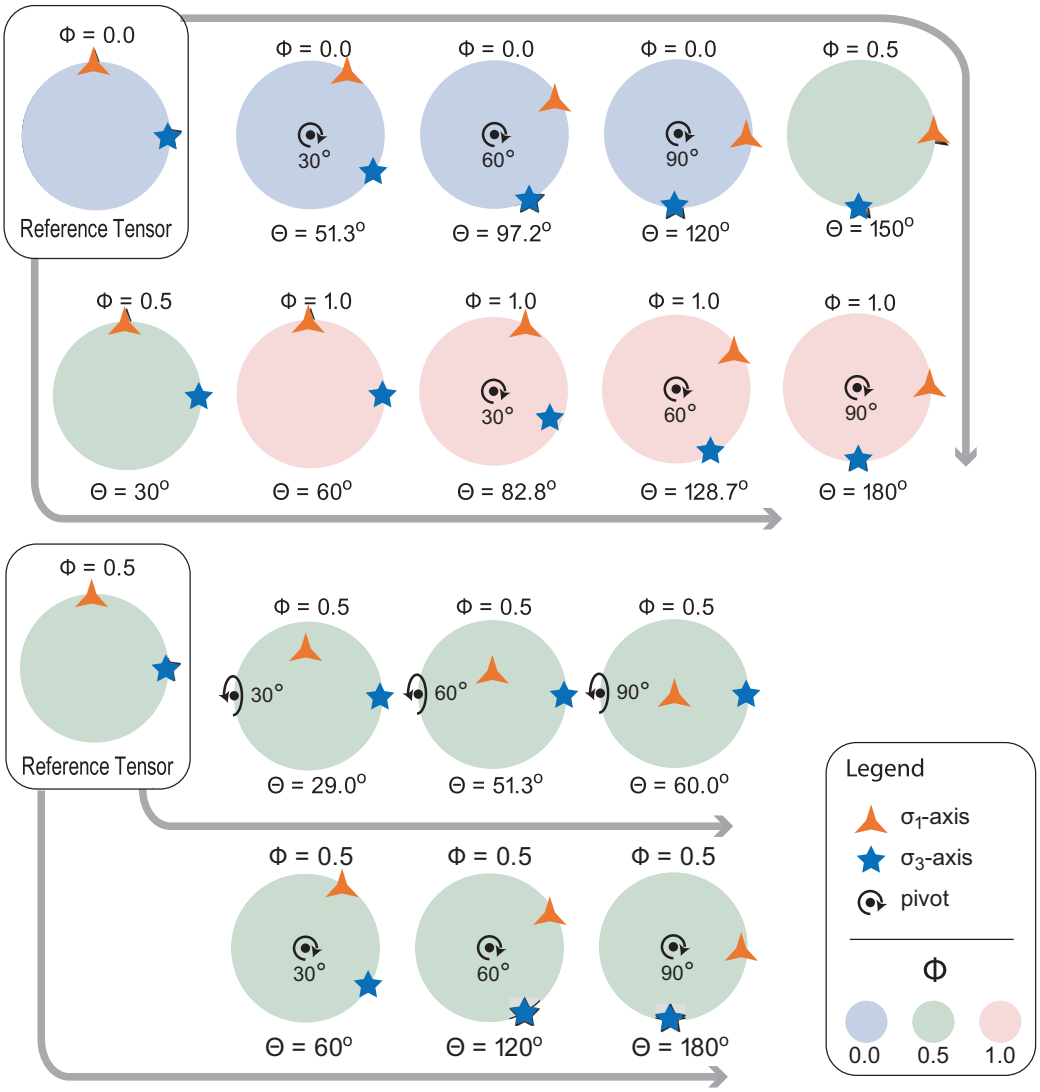


Figure 42: The angular stress distance, $\Theta$, from two reference stress states. Principal orientations are depicted by stereonets, the background colors of which indicate $\Phi$ values.

corresponded to the version-up of the main processor from version 3 to 4.

Today, the multiple inverse method uses the unit hypersphere in a five-dimensional Euclidean space as the parameter space [33]. It is important for our problem that points in the space have one-to-one correspondence with different stress states. The states have one-to-one correspondence with the reduced stress tensors defined by Eq. (6). Let us use a unit vector $\boldsymbol{x}$ with the initial point at the center of the hypersphere to denote a point on this hypersphere (Fig. 42). That is, the end-point of this vector indicates the point. Then, the one-to-one correspondence between reduced stress tensors and points on the hypersphere is expressed by the equation[12],

$$\boldsymbol{x} = \begin{pmatrix} -\left(\frac{\sqrt{2}}{4} + \frac{\sqrt{6}}{12}\right)\sigma_{11} + \left(\frac{\sqrt{2}}{4} - \frac{\sqrt{6}}{12}\right)\sigma_{22} + \frac{1}{\sqrt{6}}\sigma_{33} \\ \left(\frac{\sqrt{2}}{4} - \frac{\sqrt{6}}{12}\right)\sigma_{11} - \left(\frac{\sqrt{2}}{4} + \frac{\sqrt{6}}{12}\right)\sigma_{22} + \frac{1}{\sqrt{6}}\sigma_{33} \\ \sigma_{23} \\ \sigma_{31} \\ \sigma_{12} \end{pmatrix}, \tag{9}$$

where $\sigma_{ij}$ $(i, j = 1, 2 \text{ or } 3)$ are the components of the reduced stress tensor defined by Eq. (6). Therefore, points on the unit hypersphere have one-to-one correspondence with different stress states.

[12]Not only the components of $\boldsymbol{x}$ but also Eq. (7) guarantee the have one-to-one correspondence between $\boldsymbol{x}$ and $\boldsymbol{\sigma}$. Eq. (8) guarantees that $|\boldsymbol{x}| = 1$.

## B.5 Distance between stress states

Since stress states are represented by points on the hypersphere, it is straightforward to define distance between stress states by the angular distance between the points. That is,

$$\Theta = \arccos\left(\boldsymbol{x}^{(1)} \cdot \boldsymbol{x}^{(2)}\right).$$

We call it angular stress distance, and use the symbol $\Theta$ to denote the distance [49]. As the name suggests, $\Theta$ values range from 0° to 180° (Fig. 42).

Although $\Theta$ is defined in an abstract space, it is useful for statistics of data and of reduced stress tensors (Appendix B.6). Given two equivalent stress states, the $\Theta$ value between them equals 0°, and result in fault movements in the same direction. When $\Theta = 180°$, two stresses activate a fault in the opposite directions regardless of the fault attitude. A in-between value of $\Theta$ has an useful quantity corresponding to fault movements as well. That is, if two stress states are separated by the distance $\Theta$, the mean of the angles made by the slip directions on fault planes by those stresses is approximated very well by $\Theta$.

The rotation angle of principal stresses in the physical space is not equal with the angle $\Theta$ in the parameter space (Fig. 42). If the axial stress with $\Phi = 0$ is rotated by 90° about the line perpendicular to the symmetry axis, $\Theta$ between the stress states before and after the rotation equals 120°. If axial stresses with $\Phi = 0$ and 1 have the common stress axes, the distance between the stresses is 60°. The rotation by 30°, 60°, 90° of the triaxial stress with $\Phi = 0.5$ about the $\sigma_2$ axis correspond to the $\Theta$ values at 60°, 120°, and 180°, respectively, from the stress before the rotation.

Coordinate rotations in the physical space affects the values of $\boldsymbol{x}$ through the change in the components of $\boldsymbol{\sigma}$. However, since the parameter space is defined based on the invariants (Eqs. (7) and (8)), angular stress distance between any couples of stress states are invariant against the coordinate rotations. This means that the distance is independent from the directions of coordinate axes. Therefore, the choice of the principal orientations of the reference stress states in Fig. 42 are not responsible for the distances illustrated in this figure, although the references has E–W and N–S trending principal axes. The relative orientations of stress axes and the difference in $\Phi$ values are important.

Other than $\Theta$, stress difference $D$ [25] can be used to measure the distance between stress states. $D$ has values beteen 0 and 1, and has the one-to-one correspondence with $\Theta$ as

$$\frac{D}{2} = \sin\frac{\Theta}{2}.$$

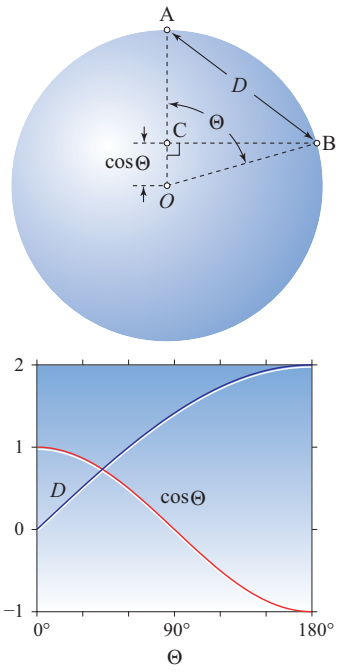


Figure 43: Distance measures between the points A and B on a unit hypersphere in a five-dimensional Euclidean space.

Instead of difference or distance, the similarity between stresses, $M$, defined by A.J. Michael [22] is sometimes used in seismology. $M$ ranges from $-1$ to 1, and is converted from $\Theta$ by the equation, $M = \cos\Theta$. Fig. 43 shows the relationships between those distance measures.

## B.6 Average and spread

The post processor calculate the average and spread of all the stress states plotted on the main window (Fig. 18). Those statistics are explained in [49].

The average is defined as follows. Given $M$ stress states, let $\boldsymbol{x}^{(1)}, \ldots, \boldsymbol{x}^{(M)}$ be the points on the hypersphere corresponding to the stress states. Then, their mean on the hypersphere is defined by the equation,

$$\overline{\boldsymbol{x}} = \frac{\boldsymbol{x}^{(1)} + \cdots + \boldsymbol{x}^{(M)}}{\left|\boldsymbol{x}^{(1)} + \cdots + \boldsymbol{x}^{(M)}\right|}.$$

The post processor shows the principal axes and stress ratio of the reduced stress tensor $\overline{\boldsymbol{\sigma}}$ corresponding to this mean vector (Fig. 18). The fact is that $\overline{\boldsymbol{\sigma}}$ is obtained directly by the component-wise mean of the

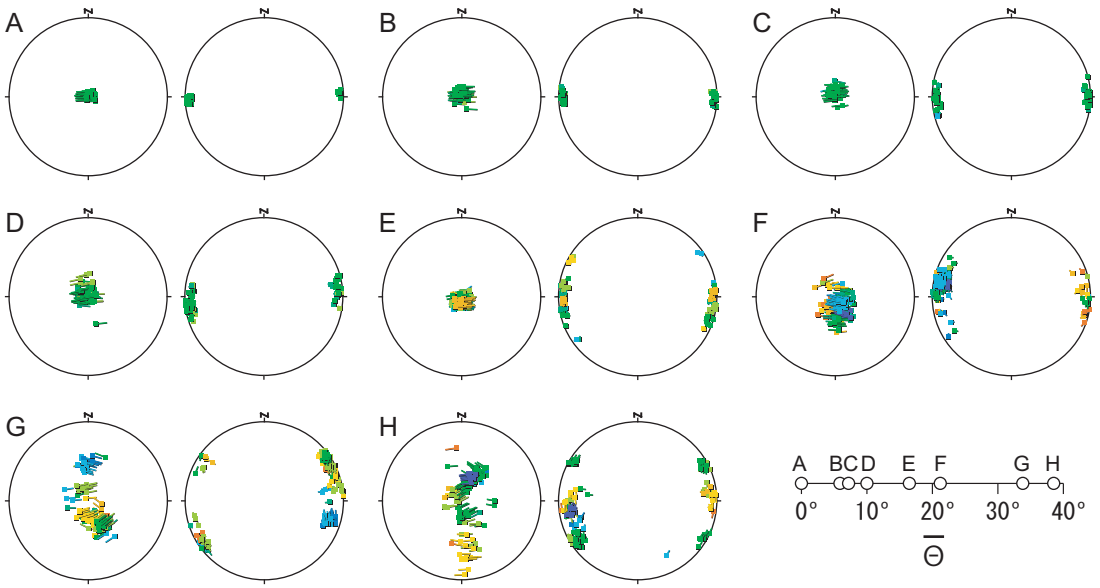


Figure 44: Dispersion of tadpole symbols and corresponding $\overline{\Theta}$ values. Enhance factor = 2.

reduced stress tensors corresponding to the given $M$ stress states, provided that the stress tensors are of the form in Eq. (6).

The spread of the $M$ stress states around the average is defined as follows. Let $\Theta^{(i)}$ be the angular stress distance of between the average and the $i$th stress states. Then, the spread is defined by the equation,

$$\overline{\Theta} = \frac{1}{M}\left[\Theta^{(1)} + \cdots + \Theta^{(M)}\right].$$

$\overline{\Theta}$ ranges from 0° to 90°. The former value indicates that all the $M$ stress states are identical. The latter indicates that the points corresponding to the stress states are uniformly distributed on the hypersphere [49]. This quantity is referred to as *mean angular stress distance* as well [49]. If a cluster of points on the hypersphere is dense and compact, $\overline{\Theta}$ has a small value, and indicates that all the stress states are similar to each other. If the stress states have a large variation, $\overline{\Theta}$ has a large value (Fig. 44).

Likewise, the mean stress difference of the $M$ stress states is defined by the equation,

$$\overline{D} = \frac{1}{M}\left[D^{(1)} + \cdots + D^{(M)}\right],$$

where $D^{(i)}$ is the stress difference between the average and the $i$th stress state. $\overline{D}$ ranges from 0 to 1. The post processor shows not only $\overline{\Theta}$ but also $\overline{D}$ (Fig. 18).

It is known that if fault-slip data are homogeneous, the noise level of the data is evaluated by $\overline{\Theta}$ [49]. That is, if observed slip directions have the errors or noises that obey a normal distribution, the standard deviation of this distribution is approximated by $\overline{\Theta}$. This is the strong point of $\overline{\Theta}$ to measure the spread of stress states for stress tensor inversion.

Although the values $\overline{\Theta} = 0$ and $\overline{D} = 0$ indicate that data have no noise and are explained by a single stress state. However, this software package rarely shows the values, because it uses discrete computational grid points to represent different stresses. For the dispersion to have the value $\overline{\Theta} = 0°$, data should have no noise, and be explained by a single state of stress. In addition, this stress should exactly correspond to one of the grid points.

It was demonstrated that a bedding tilt test like that of paleomagnetism can be conducted for paleostress studies by means of the multiple inverse method [51]. Both $\overline{\Theta}$ and $\overline{D}$ can be used for this purpose.

## B.7 Classical stress inversion

The classical stress inversion determines the optimal stress for homogeneous fault-slip data in the least-square sense, i.e., by searching the stress state that minimize misfit angles [8]. A misfit angle is evaluated by comparing the observed and theoretical slip directions of a fault, the latter of which is evaluated from Eq. (4) using a trial stress tensor. The optimal stress is determined also by maximizing

$$S = f\left(d^{(1)}\right) + \cdots + f\left(d^{(N)}\right), \qquad (10)$$

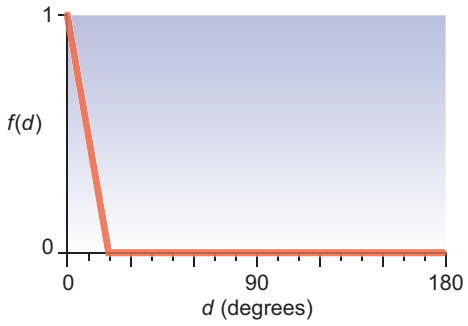


Figure 45: The function $f(d)$ used by the main processor decreases linearly from $d = 0°$ to $20°$ and keeps the constant value at 0.

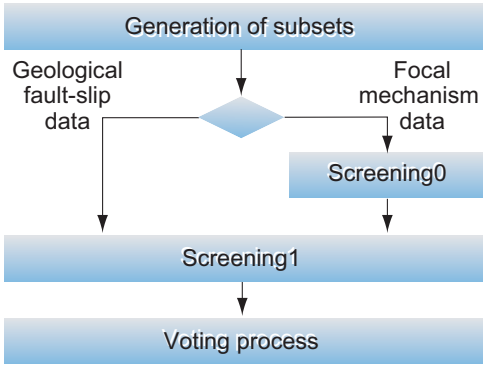


Figure 46: Data processing in the main processor.

where $d^{(i)}$ is the misfit angle of the $i$th fault, $N$ the number of fault, and $f(\,)$ is a decreasing function. The main processor uses the function shown in Fig. 45.

# C Multiple inverse method

## C.1 Computational grid points

This software package uses 60,000 stress states, which represent any stresses calculated from data. The stress states corresponds to the same number of points on the unit hypersphere in five-dimensional Euclidean space through Eq. (9). We call them the computational grid points. To optimize the resolution and efficiency of the method, the points were distributed on the hypersphere with uniform intervals using the supercomputer of Kyoto University by Sato and Yamaji [34] (Fig. 41). As as result, the 60,000 stress states were defined with "uniform intervals."

Density of the points on the hypersphere determines the precision of the method. Our points were distributed with intervals of about 10°. This corresponds to a stress difference of 0.17. The nearest neighbor distances between the points range from 7.94° to 9.51° with the average of 8.97±0.18° (one standard deviation) [50]. The precision depends not only the method but also data. If data include large noises from measurement errors, etc., the precision of the optimal stress for the data is worse than those without noises. Given homogeneous and noiseless data, the solutions of the method have the precision that is represented by the uncertainty of principal stress orientations at ~10° and that of Φ values at ~0.1. Solution is better than this precision, if the optimal stress state calculated from a given data set has the corresponding point on the hypersphere close to one of the 60,000 grid point.

## C.2 Subsets from geological fault-slip data

The multiple inverse method separates stresses from heterogeneous data by applying the classical stress inversion to the subsets of the data. All the subsets have $k$ elements, where the fault-combination number $k$ is an arbitrarily chosen by the user. The number of such subsets is, of course,

$$ {}_N\mathrm{C}_k = \frac{N!}{k!(N-k)!}. $$

Four or five are usually assigned to this parameter, and $N$ is of the order of 10 or greater. As a result, a great number of subsets are generated.

## C.3 Subsets from focal mechanism data

The problem for stress tensor inversion to deal with focal mechanism data is that it is not straightforward to distinguish which of nodal planes of a focal mechanism represent the fault plane. If the correct one is chosen from each datum, $N$ focal mechanism data are regarded as $N$ geological fault-slip data and are processed just the same way as the latter. Wrong choices lead to meaningless solutions.

The algorithm of Otsubo et al. [30] regards both the nodal planes of each focal mechanism as faults at the beginning of the processing (Fig. 27), instead of the attempt of choosing correct fault planes. And, finally, the plausibility of the hypothesis that a specific nodal plane corresponds the fault plane on which the seismic event occurred is estimated by the post processor. Therefore, ${}_{2N}\mathrm{C}_k$ subsets are generated from $N$ mechanisms.

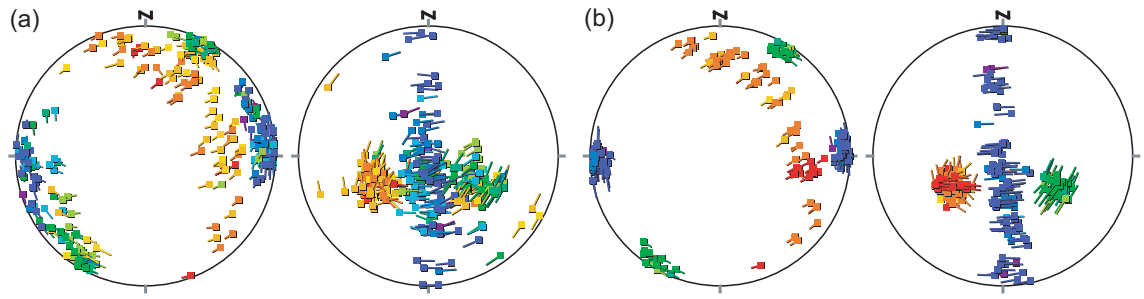


Figure 47: Paired stereograms showing the effect of Screening1 when the multiple inverse method is applied to an artificial data which were generated with assumed three stress states [47]. Results of the method (a) without and (b) with Screening1. The assumed stress states had the $\Phi$ values at 0.0, 0.5, and 1.0. Reddish and bluish tadpole symbols are distributed on great circles, because they indicate stress states with nearly axial symmetry.

### C.3.1 Screening of subsets

A part of the subsets generated by the above procedures were, then, screened out. The purpose the the screening is to reduce not only the time of computation but also noise level, and to enhance significant stresses. Subsets with unreasonable combinations of data are discarded. Subsets from focal mechanism data are filtered twice, Screening0 and Screening1, whereas the latter is applied to those from geological fault-slip data.

**Screening0** Screening0 is used only when focal mechanisms are processed (Fig. 46). $N$ focal mechanism data provides $2N$ assumed fault-slip data, from which the main processor generates ${}_{2N}\mathrm{C}_k$ subsets. However, many of those have unreasonable combinations of data in that such a subset includes both the nodal planes from an identical focal mechanism. Inversion must be applied to such data that are independent from each other. This criterion results in the 70–80% of ${}_{2N}\mathrm{C}_k$ subsets weeded out from next processing, Screening1 [30].

**Screening1** Subsets of the both data types, geological fault-slip data and focal mechanism data, are tested using the compatibility criterion of stress states and data, which is judged with misfit threshold $d_\mathrm{T} = 20^\circ$. If the misfit angle of a fault is greater than this, the fault datum is said to be incompatible or unexplained by the stress state used to calculate the misfit angle. If any stress state cannot explain all the $k$ data in a subset, the subset is said to be incompatible with the stress state. Such subsets are discarded.

Figs. 1 and 47 show the effect of Screening1. When a data set is processed without this filtering, the result of the multiple inverse method is noisy compared with the result with the filtering. Screening1 has been adopted in the main processor version 5 and later. Since the version 4 does not have this filtering, it is suitable for the bedding tilt test of paleo-stress analysis [51]. The test utilizes the heterogeneity of data.

## C.4 Voting

The subsets that have passed the screening vote for the computational grid points in the parameter space. Blue and red cards in Fig. 48 represent data from faults or focal mechanisms resulting from Stresses A and B, respectively, but we do not know the colors. All the cards are laid down on the table. In this example, we assume $k = 4$: four-element subsets of the cards are generated. If a subset passes the screening procedure, the 4 data corresponding to the 4 cards are inverted to determine the optimal state of stress for them by the classical inverse method. And, the optimal solution is represented by a computational grid point in the parameter space. Accordingly, we compare this procedure to the voting of a subset for one of the 60000 grid points, which are uniformly distributed on the unit hypersphere.

The subsets faults corresponding to blue cards vote for grid points in the vicinity of the point on the hypersphere to represent Stress A. Those corresponding to red cards vote for grid points near the point representing Stress B. However, the subsets including blue and red cards are mostly filtered out before voting. If those subsets pass the screening, they vote for variety of grid points scattered over the hypersphere. As a result, we expect that the grid points near the correct stress states get great number of votes—this is the basic idea of the multiple inverse method [46]. The post processor vi-

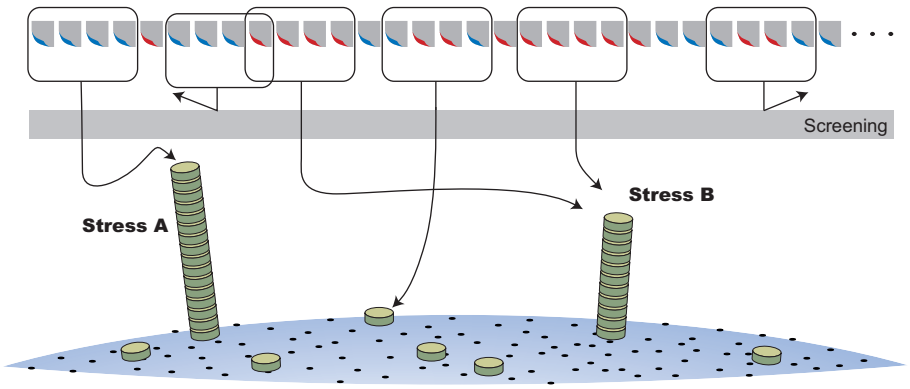


Figure 48: Schematic illustration showing the screening and voting processes of the multiple inverse method. In this figure, four-element subsets ($k = 4$) are assumed. The row of gray cards represent data. Each subset of data that has passed the screening votes for computational grid points (black dots) on the unit hypersphere (blue surface). Green boxes represent votes. Subsets of focal mechanism data are tested by Screening0 and Screening1, whereas those of geological fault-slip data only by Screening1 (Fig. 46).

sualizes the number of votes the grid points obtained.

Needless to say, the multiple inverse method can separate not only two but more stress states, if the number and qualities of data are preferable (Fig. 47). The separation is easy, if the fault planes from which the heterogeneous data were obtained have a large variety of orientations, and if the stresses have equally large numbers of data.

## C.5 Fault combination number

The main processor accepts a fault combination numbers, $k$, between 3 and 8. Which is the appropriate number? It depends on data, but we recommend $k = 5$. Fig. 49 shows the convergence of clusters made by tadpole symbols with increasing $k$ value. The figure was made with the default $e$ value. The clusters changes significantly for $k = 3$–5, but show little change for $k > 5$. Therefore, we recommend $k = 5$.

Although the stress inversion does not have a solution for $k = 3$. That is, in this case, the inversion is an under-determined problem: the number of unknown parameters, that is 4, is greater than the number of data[13].

However, the result of the present method with $k = 3$ is noisy but similar to those with $k = 4$ and greater. Why does it happen? The object function of this inversion has a maximum for $k \geq 4$, even if the function has multiple peaks [47]. The maximal point indicate the optimal solution (stress) for $k$ fault-slip data. In contrast, the function has at least one flat top for $k = 3$. Therefore, the inversion has no optimal solution. However, our main processor randomly chooses a point on the plateau. Iterating this selection many times, the method "depicts" the plateau; the plateau is visualized by scattered tadpole symbols on the paired stereograms for $k = 3$.

## C.6 Noise level of data

The multiple inverse method yields a cluster of tadpole symbols if it is applied to a homogeneous dataset with noise. From the numerical experiments, below, it is empirically known that the scatter of the cluster has a simple relationship with the noise level of the data. That is, the mean angular stress distance, $\overline{\Theta}$, of the cluster is equal to the noise level[14].

Fig. 51 shows the results of the experiments. It was assumed that misfit angles obey a normal distribution with the zero mean and the standard deviation $S_{\mathrm{d}}$. Then, the noise level was defined as the expectation of the angle:

$$\bar{p} = \int_{-\infty}^{\infty} \frac{|x|}{\sqrt{2\pi} S_{\mathrm{d}}} \exp\left(-\frac{x^2}{2S_{\mathrm{d}}^2}\right) \mathrm{d}x \approx 0.80 S_{\mathrm{d}}.$$

The experiments started from the generation of randomly oriented 50 faults, and the calculation of their theoretical slip directions to make a homogeneous dataset without noise. To this end, a reverse faulting regime of stress with E–W compression and with $\Phi = 0.5$ was assumed. Various levels of noise was

[13] A state of stress has four degrees of freedom, three for the attitude of stress ellipsoid and one for $\Phi$.

[14] The bootstrap solutions from noisy homogeneous data have such a simple relationship [49].

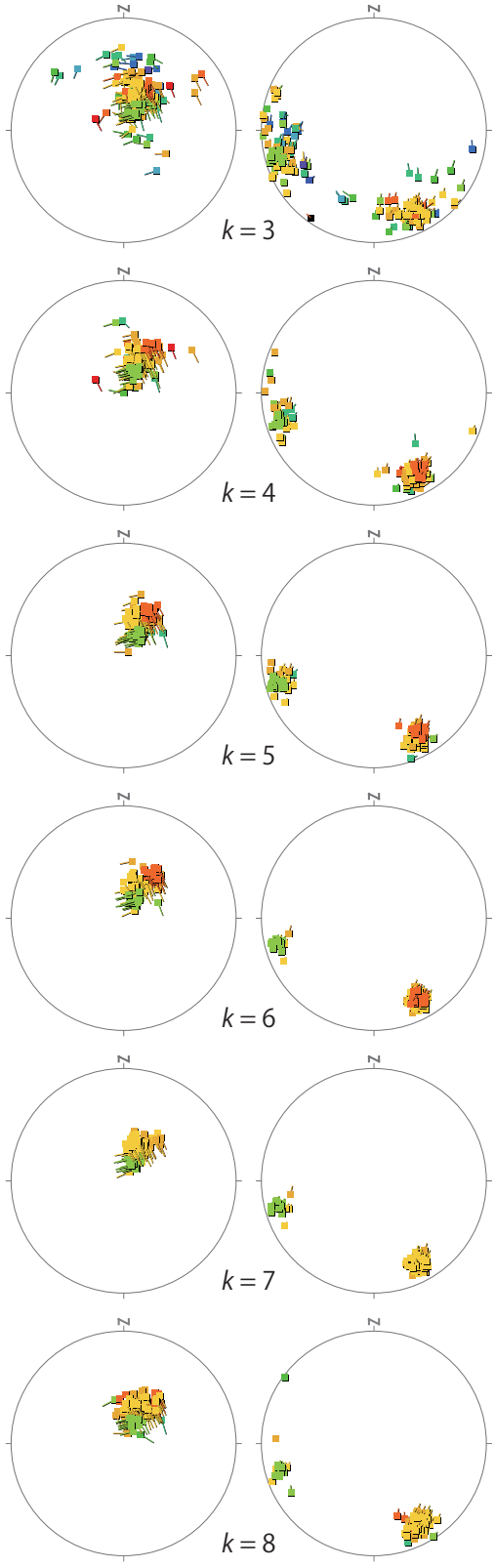


Figure 49: Results of the multiple inverse method applied to the same artificial dataset but with different $k$ values.

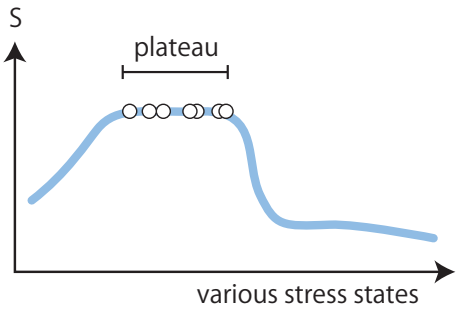


Figure 50: Schematic illustration for the object function $S(\sigma)$ of the stress inversion for $k = 3$. In this case, the function does not have a sharp peak but a flat top. Open circles represent the stress states indicated by tadpole symbols.

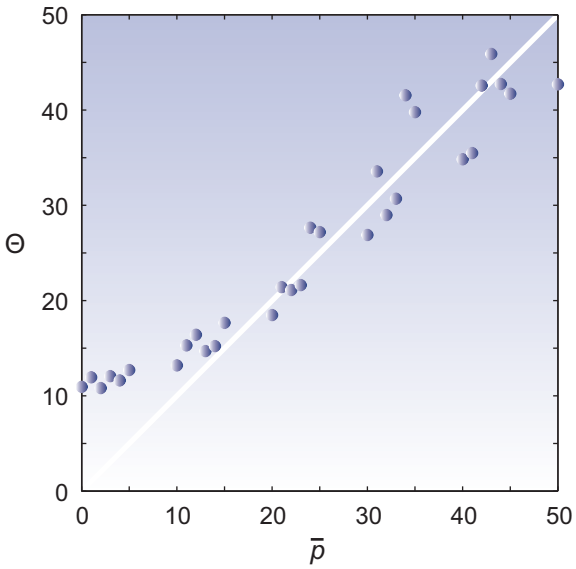


Figure 51: Mean angular stress distances for the results of the present method applied to the same homogeneous data with various noise levels. The level is denoted by $\bar{p}$. The distances were measured with the default enhanced factor.

added to the data to make artificial datasets (Fig. 52). The mean angular stress distance, $\overline{\Theta}$ was calculated for the cluster obtained by the multiple inverse method from each dataset. Fig. 51 demonstrates that if the noise level is greater than 15–20°, $\overline{\Theta}$ is roughly equal to the noise level. However, this relationship does not hold for smaller noise levels. As the level become smaller, $\overline{\Theta}$ does not vanish but approaches ~10°. This deviation results from the use of computational grid points, the intervals of which are ~10° [50]. When the grid points were not used but bootstrap solutions were evaluated, the cluster of the solutions vanished

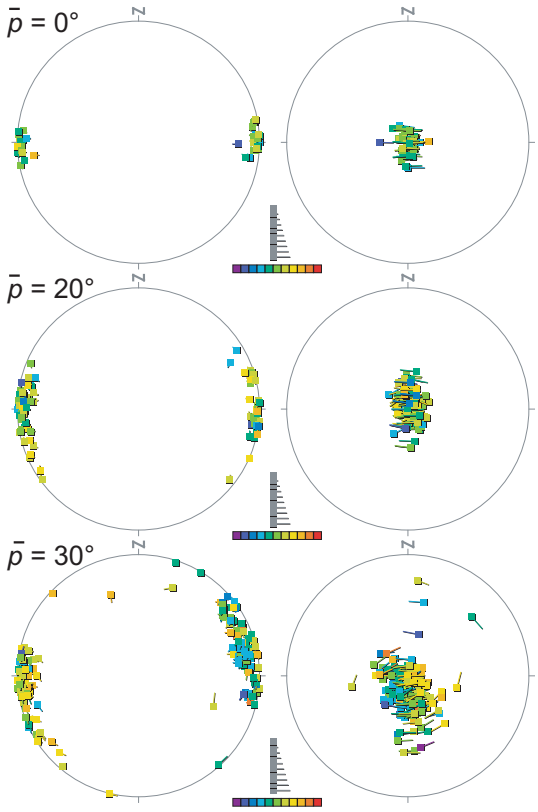


Figure 52: Results of the present method applied to homogeneous data with three noise levels. Paired stereograms were drawn with the default enhance factor ($e$ = 8).

with $\bar{p}$ [49].

In conclusion, the mean angular stress distance of the cluster obtained through the present method from a homogeneous dataset indicates the noise level of the data[15], if $\overline{\Theta}$ is greater than 15–20°. If $\overline{\Theta}$ is smaller than that, the noise level is smaller than $\overline{\Theta}$.

# D Default colors for stress ratios

Colors of tadpole symbols denote stress ratios in the main window of MI Viewer. Their default color palette was changed when the post processor was upgraded from version 4.15 to 4.16 (Table 3). The difference can cause a problem if figures maded by the old and new versions are combined.

[15]The numerical experiments assumed that misfit angles obeyed a normal distribution, but it is not clear what kind of statistical distribution they really obey.

Table 3: The RGB values of the default colors of tadpole symbols in the Main Window to denote stress ratios. The RGB values with gray background were changed when the main processor was upgraded from ver. 4.15 to 4.16.

| Φ | Old | | | New | | |
|---|---|---|---|---|---|---|
| | R | G | B | R | G | B |
| 0.0 | 120 | 0 | 255 | 120 | 0 | 255 |
| 0.1 | 70 | 66 | 247 | 70 | 66 | 247 |
| 0.2 | 46 | 110 | 245 | 46 | 110 | 245 |
| 0.3 | 76 | 173 | 204 | 76 | 173 | 204 |
| 0.4 | 18 | 204 | 123 | 18 | 204 | 123 |
| 0.5 | 20 | 213 | 20 | 118 | 208 | 28 |
| 0.6 | 143 | 216 | 27 | 194 | 214 | 27 |
| 0.7 | 255 | 217 | 1 | 237 | 225 | 10 |
| 0.8 | 242 | 181 | 16 | 242 | 181 | 16 |
| 0.9 | 245 | 102 | 15 | 245 | 102 | 15 |
| 1.0 | 237 | 0 | 18 | 237 | 0 | 18 |

# E List of mathematical symbols

| | |
|---|---|
| $D$ | stress difference |
| $\overline{D}$ | mean stress difference |
| $d$ | misfit angle |
| $d_{\mathrm{T}}$ | misfit threshold |
| $k$ | fault combination number |
| $N$ | number of data |
| $N_{\mathrm{G}}$ | number of computational grid points |
| $N_{\mathrm{p}}$ | number of plotted stress states |
| $\boldsymbol{x}$ | unit vector in 5-dimensional Euclidean space representing a state of stress |
| $\overline{\boldsymbol{x}}$ | unit vector corresponding to the average stress states |
| $\Theta$ | angular stress distance |
| $\overline{\Theta}$ | mean angular stress distance |
| $\boldsymbol{\sigma}$ | reduced stress tensor |
| $\overline{\boldsymbol{\sigma}}$ | average stress state |
| $\sigma_1$ | maximum principal stress |
| $\sigma_2$ | intermediate principal stress |
| $\sigma_3$ | minimum principal stress |
| $\Phi$ | stress ratio |

# References

[1] Angelier, J., 1979. Determination of the mean principal directions of stresses for a given fault population. *Tectonophysics*, **5**, T17–T26.

[2] Angelier, J., 1984. Tectonic analysis of fault slip data sets. *Journal of Geophysical Research*, **89**, 5835–5848.

[3] Angelier, J., 1994. Fault slip analysis and paleostress reconstruction. In, Hancock, P. L., ed., *Continental deformation*, Pergamon Press, Oxford, 53–101.

[4] Awaji, D., Yamajoto, D. and Takagi, H., 2006. Kinematic history of the Tanakura Shear Zone at brittle regime. *Journal of Geological Society of Japan*, **112**, 222–240.

[5] Ballard, D.H. 1981. Generalizing the Hough transform to detect arbitrary shapes. *Pattern Recognition*, **13**, 111–122.

[6] Borradaile, G.J., 2003. *Statistics of Earth Science Data: Their Distribution in Time, Space, and Orientation*. Springer-Verlag, Berlin.

[7] Bott, M.H.P., 1959. The mechanics of oblique slip faulting. *Geological Magazine*, **96**, 109–117.

[8] Carey, E. and Brunier, B., 1974. Analyse théorique et numérique d'un modèle mécanique élémentaire appliqué à l'étude d'une population de failles. *Comptes Rendus de l'Académie des Sciences, Paris, Serie D.*, **279**, 891–894.

[9] Eliassi, M. and Ahmadian, S., 2007. Determination of the geometrical configuration of $\sigma_1$ trajectory in Kan-Karaj area (Central Alborz) using Multiple Inverse Method. *Geosciences*, **67**, 140–149.

[10] Eliassi, M., Mohajjel, M. and Mesbahi, F., 2008. Paleostress analysis of horizontal Plio-Quaternary deposits in the NW of Zanjan. *Journal of Earth and Space Physics*, **34**, 27–42.

[11] Gephart, J.W. and Forsyth, D.W., 1984. An improved method for determining the regional stress tensor using earthquake focal mechanism data: Application to the San Fernando earthquake sequence. *Journal of Geophysical Research*, **89**, 9305–9320.

[12] Havíř, J. and Gilíková, 2007. Results of the structural study of the Culm sediments near Suchdol and Odrou. *Geological Research in Moravia and Silesia*, **14**, 52–55.

[13] Hiratsuka, S. and Sato, T., 2008. Application of the multiple inverse method to estimating the stress field in and around the rupture zone of the 2004 Sumatra-Andaman Earthquake. *Journal of the Seismological Society of Japan*, **61**, 61–75.

[14] Ishii, E., Yasue, K., Takenobu, T., Tsukuwi, R., Matsuo, K., Sugiyama, K. and Matsuo, S., 2006. Three-dimensional distribution and hydrogeological properties of the Omagari Fault in the Horonobe area, northern Hokkaido, Japan. *Journal of Geological Society of Japan*, **112**, 301–314.

[15] Ishii, E. and Fukushima, T., 2006. A case study of analysis of faults in Neogene siliceous rocks. *Journal of the Japan Society of Engineering Geology*, **47**, 280–291.

[16] Ishii, E., Sanada, H., Funaki, H., Sugita, Y. and Kurikami, H., 2011. The relationships among brittleness, deformation behavior, and transport properties in mudstones: An example from the Horonobe Underground Research Laboratory, Japan. *Journal of Geophysical Research*, **116**, B09206.

[17] Kuniyasu, M. and Yamada, Y., 2004. Structural analysis of deep zones in southern central Hokkaido, northern Japan. *Journal of the Japanese Association for Petroleum Technology*, **69**, 131–144.

[18] Kusuhashi, N. and Yamaji, A., 2001. Miocene tectonics of SW Japan as inferred from the Kuma Group, Shikoku. *Journal of Geological Society of Japan*, **107**, 25–40.

[19] Liesa, C.L., Lisle, R.J., 2004. Reliability of methods to separate stress tensors from heterogeneous fault-slip data. *Journal of Structural Geology*, **26**, 559–572.

[20] Lunina, O.V. and Gladkov, A.S., 2008. Active faults and crustal stress in the northeastern flank of the Baikal rift system. *Russian Geology and Geophysics*, **49**, 113–123.

[21] Lunina, O.X., Gladkov, A.S., Novikov, I.S., Agatova, A.R., Vysotskii, E.Y. and Emanov, A.A., 2008. Geometry of the fault zone of the 2003 Ms = 7.5 Chuya earthquake and associated stress fields, Gorny Altai. *Tectonophysics*, **453**, 276–294.

[22] Michael, A.J., 1987. Use of focal mechanisms to determine stress: A control study. *Journal of Geophysical Research*, **92**, 357–368.

[23] Minamizawa, S., Kuwano, K., Sakaguchi, A. and Hashimoto, Y., 2006. Structural and paleostress analysis of Muroto formation, the Tertiary Shimanto Complex, Shikoku. *Japanese Journal of Structural Geology*, **49**, 87–98.

[24] Morris, A., Ferrill, D.A. and Henderson, D.B., 1996. Slip-tendency analysis and fault reactivation. *Geology*, **24**, 275–278.

[25] Orife, T. and Lisle, R.J., 2003. Numerical processing of palaeostress results. *Journal of Structural Geology*, **25**, 949–957.

[26] Osozawaa, O. and Pavlis, T., 2007. The high P/T Sambagawa extrusional wedge, Japan. *Journal of Structural Geology*, **29**, 1131–1147.

[27] Otsubo, M., Sato, K. and Yamaji, A., 2006. Computerized identification of stress tensors determined from heterogeneous fault-slip data by combining the multiple inverse method and k-means clustering. *Journal of Structural Geology*. **28**, 991–997.

[28] Otsubo, M., Shigematsu, N., Kitagawa, Y. and Koizumi, N., 2009. Stress history in the forearc region of the Nankai trough subduction zone: paleostress analysis based on faults in core samples from the Kumano Ichiura and Kihoku Miyama sites, Kii Peninsula, SW Japan. *Journal of Geological Society of Japan*, **115**, 457–469.

[29] Otsubo, M. and Yamaji, A., 2006. Improved resolution of the multiple inverse method by eliminating erroneous solutions. *Computers & Geosciences*, **32**, 1221–1227.

[30] Otsubo, M., Yamaji, A. and Kubo, A., 2008. Determination of stresses from heterogeneous focal mechanism data: An adaptation of the multiple inverse method. *Tectonophysics*, **457**, 150–160.

[31] Pasquale, G., De Matteis, R., Romeo, A. and Maresca, R., 2009. Earthquake focal mechanisms and stress inversion in the Irpinia Region (southern Italy). *Journal of Seismology*, **13**, 107–124.

[32] Pêcher, A., Seeber, L., Guillot, S., Jouanne, F., Kausar, A., Latif, M., Majid, A., Mahéo, G., Mugnier, J.L., Rolland, Y., van der Beek, P. and Van Melle, J., 2008. Stress field evolution in the northwest Himalayan syntaxis, northern Pakistan. *Tectonics*, **27**, TC6005.

[33] Sato, K. and Yamaji, A., 2006a. Embedding stress difference in parameter space for stress tensor inversion. *Journal of Structural Geology*, **28**, 957–971.

[34] Sato, K. and Yamaji, A., 2006b. Uniform distribution of points on a hypersphere for improving the resolution of stress tensor inversion. *Journal of Structural Geology*, **28**, 972–979.

[35] Sippel, J., Scheck-Wenderoth, M., Reicherter, K. and Mazur, S., 2009. Paleostress states at the south-western margin of the Central European Basin System—Application of fault-slip analysis to unravel a polyphase deformation pattern. *Tectonophysics*, 470, 129–146.

[36] Tomita, S. and Yamaji, A., 2001. Are paleostress estimations assuming conjugate faulting always faulty? Comparison with the multiple inverse method using fault-slip data from the Niitsu Hill, Niigata Prefecture, Japan. *Journal of Geological Society of Japan*, **107**, 711–721.

[37] Tomita, S. and Yamaji, A., 2003. KUT: Software to rotate orientation data. *Geoinformatics*, **14**, 85–104.

[38] Twiss, R.J. and Moores, E.M., 1992. *Structural Geology*, W.H. Freeman, New York.

[39] Vaola, G., Ganerod, G.V. and Wahlgren, C.H., 2009. Unraveling 1.5 Ga of brittle deformation history in the Laxemar-Simpevarp area, southeast Sweden: A contribution to the Swedish site investigation study for the disposal of highly radioactive nuclear waste. *Tectonics*, **28**, TC5007, doi:10.1029/2009TC002461.

[40] Vasseur, G., Etchecopar, A. and Philip, H., 1983. Stress state inferred from multiple focal mechanisms. *Annales Geophysicae*, **1**, 291–298.

[41] Veloso, E.E., Anma, R. and Yamaji, A., 2009. Ophiolite emplacement and the effects of the subduction of the active Chile Ridge System: Heterogeneous paleostress regimes recorded on the Taitao Ophiolite (southern Chile). *Andean Geology*, **36**, 3–16.

[42] Viola, G., Venvik Ganerød, G. and Wahlgren, C.-H., 2009. Unraveling 1.5 Ga of brittle deformation history in the Laxemar-Simpevarp area, southeastern Sweden: A contribution to the Swedish site investigation study for the disposal of highly radioactive nuclear waste. *Tectonics*, **28**, TC5007.

[43] Wallace, R. E., 1951. Geometry of shearing stress and relationship to faulting. *Journal of Geology*, **59**, 111–130.

[44] Yamada, Y. and Yamaji, A., 2002. Determination of paleo-stresses from mesoscale shear fractures in core samples using the multi-inverse method. *Journal of Petroleum Geology*, **25**, 203–218.

[45] Yamaji, A., 2000a. Multiple inverse method applied to mesoscale faults in mid Quaternary sediments near the triple trench junction off central Japan. *Journal of Structural Geology*, **22**, 429–440.

[46] Yamaji, A., 2000b. The multiple inverse method: a new technique to separate stresses from heterogeneous fault-slip data. *Journal of Structural Geology*, **22**, 441-452.

[47] Yamaji, A., 2003. Are the solutions of stress inversion correct? Visualization of their reliability and the separation of stresses from heterogeneous fault-slip data. *Journal of Structural Geology*, **25**, 241–252.

[48] Yamaji, A., Otsubo, M. and Sato, K., 2006. Paleostress analysis using the Hough transform for separating stresses from heterogeneous fault-slip data. *Journal of Structural Geology*, **28**, 980–990.

[49] Yamaji, A. and Sato, K., 2006. Distances for the solutions of stress tensor inversion in relation to misfit angles that accompany the solutions. *Geophysical Journal International*, **167**, 913–942.

[50] Yamaji, A. and Sato, K., 2011. A spherical code and stress tensor inversion. *Computers & Geosciences*, in press. doi:10.1016/j.cageo.2011.04.016.

[51] Yamaji, A., Tomita, S. and Otsubo, M., 2005. Bedding tilt test for paleostress analysis. *Journal of Structural Geology*, **27**, 161–170.

# Index